nature structural & molecular biology

Article

https://doi.org/10.1038/s41594-023-01000-z

Intrinsic mesoscale properties of a Polycomb protein underpin heterochromatin fidelity

Received: 28 March 2022

Accepted: 17 April 2023

Published online: 22 May 2023

Check for updates

Sujin Lee[1], Stephen Abini-Agbomson[2], Daniela S. Perry[1], Allen Goodman[3], Beiduo Rao[1], Manning Y. Huang[1], Jolene K. Diedrich[4], James J. Moresco[4], John R. Yates III[4], Karim-Jean Armache[2] & Hiten D. Madhani[1,5]

Little is understood about how the two major types of heterochromatin domains (HP1 and Polycomb) are kept separate. In the yeast *Cryptococcus neoformans*, the Polycomb-like protein Ccc1 prevents deposition of H3K27me3 at HP1 domains. Here we show that phase separation propensity underpins Ccc1 function. Mutations of the two basic clusters in the intrinsically disordered region or deletion of the coiled-coil dimerization domain alter phase separation behavior of Ccc1 in vitro and have commensurate effects on formation of Ccc1 condensates in vivo, which are enriched for PRC2. Notably, mutations that alter phase separation trigger ectopic H3K27me3 at HP1 domains. Supporting a direct condensate-driven mechanism for fidelity, Ccc1 droplets efficiently concentrate recombinant *C. neoformans* PRC2 in vitro whereas HP1 droplets do so only weakly. These studies establish a biochemical basis for chromatin regulation in which mesoscale biophysical properties play a key functional role.

Heterochromatin has numerous critical biological roles including genome defense, gene regulation, developmental memory and centromere function[1,2]. Among the best-studied forms of heterochromatin are those programmed by HP1 and Polycomb systems, which are respectively characterized by chromatin harboring methylation of the amino-terminal histone H3 tail on lysine 9 (H3K9) or lysine 27 (H3K27)[2]. Coupling of recognition of these marks by 'readers' of these modifications and the cognate methyltransferases is critical for the formation and maintenance of heterochromatin domains[1,2]. However, exactly how heterochromatin is established and inherited in vivo is not yet well understood. Heterochromatic DNA and heterochromatic proteins have long been known to form subnuclear structures, raising the possibility that mesoscale organization plays a functional role.

A potential role for protein phase separation in this organization has been proposed based on recent studies in which HP1a/α proteins from humans and *Drosophila* were found to form condensates via phase separation in vitro[3,4]. These studies also showed that human HP1α can compact DNA in vitro and that *Drosophila* HP1a displays the properties of a liquid in early *Drosophila* embryos[3,4]. Likewise, CBX2, a core subunit of the human canonical PRC1 complex that recognizes H3K27 trimethylation (H3K27me3) and harbors a functionally important positively charged disordered region long known to mediate chromatin compaction in vitro[5,6], has recently been shown to undergo phase separation in a manner that correlates with the formation of foci of green fluorescent protein (GFP)-tagged CBX2 in transduced fibroblasts[7–9]. These and other studies have led to increasing interest in the hypothesis that phase separation of heterochromatin readers and associated factors mediated by multivalent intermolecular interactions has critical functional roles in heterochromatin[10–13]. However, there is debate in the field about the in vivo function and relative importance of the phase separation behavior of heterochromatin readers[14]. Also not yet addressed is the critical question of how phase separation contributes to maintenance of different heterochromatin domains (for example, H3K9me3 versus H3K27me3 domains).

We previously described the first yeast Polycomb system, in the basidiomycete yeast *C. neoformans*[15]. This system silences subtelomeric

[1]Department of Biochemistry and Biophysics, University of California, San Francisco, CA, USA. [2]Department of Biochemistry and Molecular Pharmacology, New York University Grossman School of Medicine, New York, NY, USA. [3]Broad Institute of MIT and Harvard, Cambridge, MA, USA. [4]Department of Molecular Medicine, The Scripps Research Institute, La Jolla, CA, USA. [5]Chan-Zuckerberg Biohub, San Francisco, CA, USA. e-mail: hitenmadhani@gmail.com

domains via methylation of H3K27 by a PRC2-like complex. We identified a Polycomb-like reader protein we named Ccc1 (chromodomain protein harboring a coiled-coil region), the genetic deletion of which resulted in a notable phenotype: the ectopic deposition of H3K27me3 at centromeric HP1 domains marked by H3K9me. This ectopic deposition was lost in cells in which H3K9me was removed by deletion of the enzyme responsible for this mark, Clr4/Suv39h. We concluded that the PRC2 complex has a latent promiscuity that allows it to be attracted to HP1 domains, but this is suppressed by Ccc1 (ref. 15).

In the present study, we report this fidelity function of Ccc1 requiring its ability to undergo phase separation. We find that Ccc1, which harbors a large intrinsically disordered region (IDR) with multiple positively and negatively charged amino acid clusters and a coiled-coil domain, readily undergoes phase separation in vitro. By constructing a series of mutations in charge clusters in the IDR of Ccc1, and also by removing its coiled-coil domain (which we show is a dimerization domain), we map the determinants of its in vitro behavior, identifying mutants that markedly reduce phase separation propensity in vitro, increase it or leave it unchanged. We show that Ccc1 forms subnuclear foci in vivo which concentrate PRC2 and, by precise gene replacement tagging and super-resolution microscopy, we show that the in vitro phenotypes of the mutations faithfully predict their effect on the formation of bright foci in cells. Importantly, mutants that alter phase separation in vitro and focus formation in vivo result in promiscuous deposition of H3K27me3 at centromeres, whereas mutants that do not impact condensate formation behave as wild-type. By expressing and purifying a recombinant *C. neoformans* PRC2 complex, we show that Ccc1 droplets concentrate PRC2 in vitro, whereas Swi6/HP1 droplets do so only weakly, correlating with the ectopic deposition of H3K27me3 at HP1 domains in the absence of Ccc1. Ccc1 protein within droplets displays no detectable mobility yet forms spherical structures that fuse. PRC2 concentrated in these droplets displays mobility on minute timescales. Both are considerably less dynamic than condensate-resident HP1, indicating distinctive viscoelastic properties. This work establishes a functional role for the intrinsic mesoscale properties of a chromatin reader protein in promoting the fidelity of heterochromatin domain organization.

Results

Ccc1 forms phase-separated condensates in vitro

Our previous studies identified the first yeast Polycomb system in *C. neoformans* in which deposition of H3K27me3 in subtelomeric domains triggers gene repression[15]. Based on reciprocal affinity purification and mass spectrometry (AP–MS) experiments, we identified a *C. neoformans* PRC2 complex containing five subunits (Ezh2, Eed1, Bnd1, Msl1 and Ccc1). Three of the PRC2 complex members, Ezh2, Eed1 and Msl1, are clear orthologs of canonical PRC2 subunits, whereas Bnd1 (big protein with no domains) and Ccc1 are fungal specific. Ccc1 harbors an N-terminal chromodomain which binds H3K27me3. Notably, loss of Ccc1 or mutation of its chromodomain results in the ectopic formation of H3K27me3 islands at HP1-marked regions[15]. Based on these data, we proposed that the anchoring of the PRC2 complex to sites of previous action via Ccc1 is required for heterochromatin fidelity (Fig. 1a)[15].

In the process of performing additional AP–MS experiments, we observed that the capture of PRC2 during purification of tagged Ccc1 was entirely DNA-dependent, being lost if extracts were treated with DNase before purification; the converse was true when Ezh2 was used as the bait (Extended Data Fig. 1a–c). These findings indicated that Ccc1 is not a tightly bound core subunit of PRC2 and raised the question of how Ccc1 could effectively anchor PRC2 to sites of its previous action. Given recent work on phase separation of heterochromatin readers[3,4,7,8], we hypothesized that Ccc1 might form condensates that organize H3K27me3-marked heterochromatin domains (Fig. 1b). Supporting this possibility, Ccc1 contains a large predicted IDR between its chromodomain and a predicted α-helical coiled-coil region (Fig. 1c,d), both of which can drive multivalent interactions required for phase separation[16–18]. We expressed and purified 6xHis-tagged wild-type Ccc1 and a truncated version missing the predicted carboxyl-terminal coiled-coil (Ccc1-CCΔ) in *Escherichia coli* (Extended Data Fig. 2a). We found that full-length Ccc1 precipitates in a buffer that contains ≤150 mM NaCl, indicating that the protein solubility is compromised by low salt concentration. Mass photometry analysis showed that the purified 6xHis-Ccc1 (predicted mass: 112 kDa) can dimerize (measured mass: 210 ± 17.4 kDa) whereas the coiled-coil deletion (1–434 amino acids, predicted mass: 50.3 kDa) is a monomer (measured mass: 55 ± 9.2 kDa) (Extended Data Fig. 2b,c). Solutions of full-length Ccc1 became turbid on lowering of NaCl concentration from 500 mM to 250 mM (Fig. 1e). Microscopic observation revealed concentration-dependent formation of spherical Ccc1 condensates in 20 mM HEPES, pH 7.5, and 250 mM NaCl (Fig. 1f and Extended Data Fig. 3a). No crowding agents were required. Ccc1 condensates fused and grew over time, consistent with a liquid-like state (Fig. 1g and Supplementary Video 1). Adding 10% (w:v) 1,6-hexanediol, an aliphatic alcohol that weakens hydrophobic interactions driving phase separation[19], inhibited condensate formation (Fig. 1h). Nuclease treatment of purified Ccc1 and addition of DNA did not impact condensate formation (Extended Data Fig. 3b,c). Ccc1 condensates formed at 150 mM NaCl appeared less liquid-like, consistent with the reduced solubility observed during purification (Extended Data Fig. 3d). To test whether the formation of Ccc1 condensates is reversible, we increased NaCl concentration from 250 mM to 500 mM and found that they immediately dissolved (Extended Data Fig. 3e). Further supporting reversibility, we observed that irregular condensates, which formed at 150 mM NaCl, recovered a spherical shape when the NaCl concentration was increased to 250 mM (Extended Data Fig. 3f). We conclude that Ccc1 undergoes phase separation in vitro.

IDR and coiled-coil program phase separation of Ccc1

Depending on the protein, phase separation can be driven by networks of physical crosslinks that include electrostatic, cation-π and/or hydrophobic interactions between disordered protein segments, as well as more conventional binding between folded domains such as those mediated by coiled-coils[17,20–23]. The Ccc1 IDR contains several prominent clusters of tandem charged residues of the same polarity (Fig. 2a and Extended Data Fig. 4a,b). To investigate whether the electrostatic properties derived from these clusters influence Ccc1 condensate formation, we replaced the charged residues in the two basic and the two acidic clusters to alanine (Fig. 2a). The first mutant, 4KRA, alters a four-residue cluster just downstream of the chromodomain and is 24 residues upstream of the second cluster which harbors 6 tandem basic residues that we also mutated to alanine residues (6KRA). To test whether there might be an additive effect, we combined these two mutants to make a mutant that we term 10KRA. Two mutants that alter clusters of acidic residues, 4DEA and 5DEA, were also combined to make a third mutant that we refer to as 9DEA. As discussed earlier, Ccc1 dimerizes whereas the C-terminally truncated mutant Ccc1 (Ccc1-CCΔ, 1–434 amino acids) is monomeric (Extended Data Fig. 2b,c).

We tested phase separation of the purified proteins (6.7 µM; Extended Data Fig. 2a,d) by lowering NaCl concentration from 500 mM to 250 mM at room temperature for up to 2 h (Fig. 2b and Extended Data Fig. 4c). We found that the 6KRA and 10KRA proteins displayed defects in phase separation. We confirmed our microscopic observations by quantifying the number of condensates observed in a field for each Ccc1 variant after 30 min of induction (Fig. 2c). We could not obtain liquid-like, phase-separated condensates of Ccc1-CCΔ under these conditions. Even on increasing protein concentration to 85 µM, this mutant formed irregular condensates only at a much slower rate (Fig. 2d), indicating that phase separation propensity is perturbed. We also measured turbidity of Ccc1 variants; the results were consistent with our microscopic observations. The 6KRA and 10KRA mutants exhibited reduced turbidity compared with wild-type and Ccc1-CCΔ did not become turbid at all (Fig. 2e).

https://doi.org/10.1038/s41594-023-01000-z

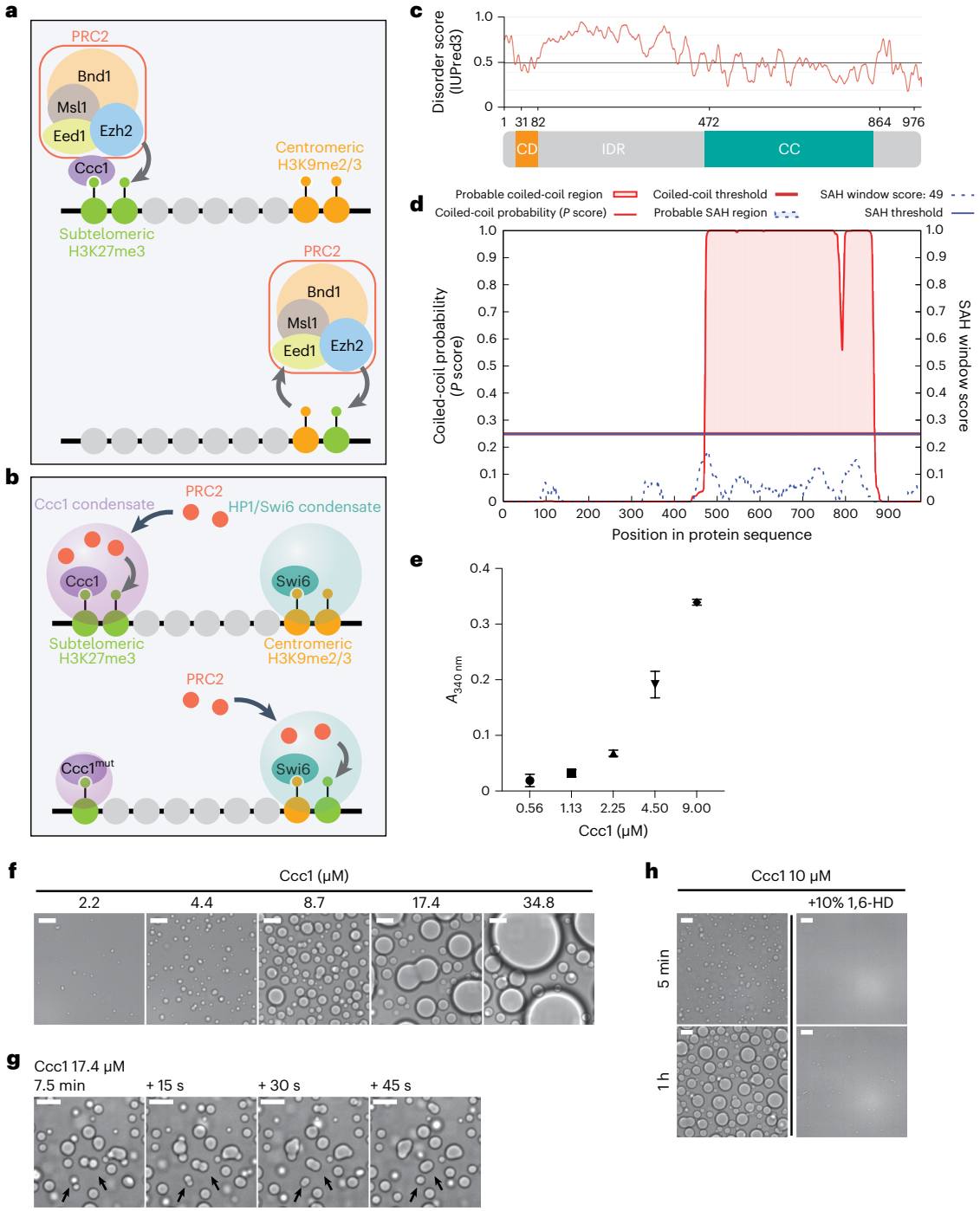

Fig. 1 | *C. neoformans* H3K27me3 reader protein Ccc1 undergoes phase separation in vitro. a, Top, model for the role of product recognition of Ccc1 in keeping PRC2 at subtelomeres; bottom, in a *ccc1Δ* or chromodomain mutant, PRC2 recognizing H3K9me2/3 instead and redistributing H3K27me3 to centromeres. **b**, Model for the role of phase separation for PRC2 partitioning. **c**, Prediction of disordered and structured domains of Ccc1. CC, coiled coil; CD, chromodomain; IDR, intrinsically disordered region. **d**, Prediction of coiled-coil and single α-helices (SAHs) in Ccc1. **e**, Turbidity measurements of Ccc1 at indicated protein concentration. Phase separation was induced for 30 min at room temperature, 20 mM HEPES, pH 7.5, and 250 mM NaCl, and absorbance at 340 nm ($A_{340\,nm}$) was measured at 25 °C (mean ± s.d., $n = 3$ independent replicates). **f**, Differential interference contrast (DIC) microscopy images of Ccc1 condensates at indicated protein concentration. Phase separation was induced at room temperature, 20 mM HEPES, pH 7.5 and 250 mM NaCl, and images were obtained after 1 h. Scale bars, 10 μm. **g**, Condensate fusion of 17.4 μM Ccc1 at indicated time points. Scale bars, 10 μm. **h**, Disruption of 10 μM Ccc1 condensates by 10% (w:v) 1,6-hexanediol (1,6-HD). Scale bars, 10 μm. Data represent three (**f** and **g**) or two (**h**) independent experiments.

We noticed that, over time, the 4KRA mutant developed condensates with elongated shapes (Fig. 2b and Extended Data Fig. 4c), indicating that material properties may be altered in this mutant. All condensates are likely to be viscoelastic network fluids[24] and mutations may influence the balance between the viscous and the elastic properties of condensates[22]. It has been shown that phase transitions of multivalent proteins and nucleic acids involve a coupling between phase separation and gelation[25]. The closer the equilibrium dense phase concentration is

https://doi.org/10.1038/s41594-023-01000-z

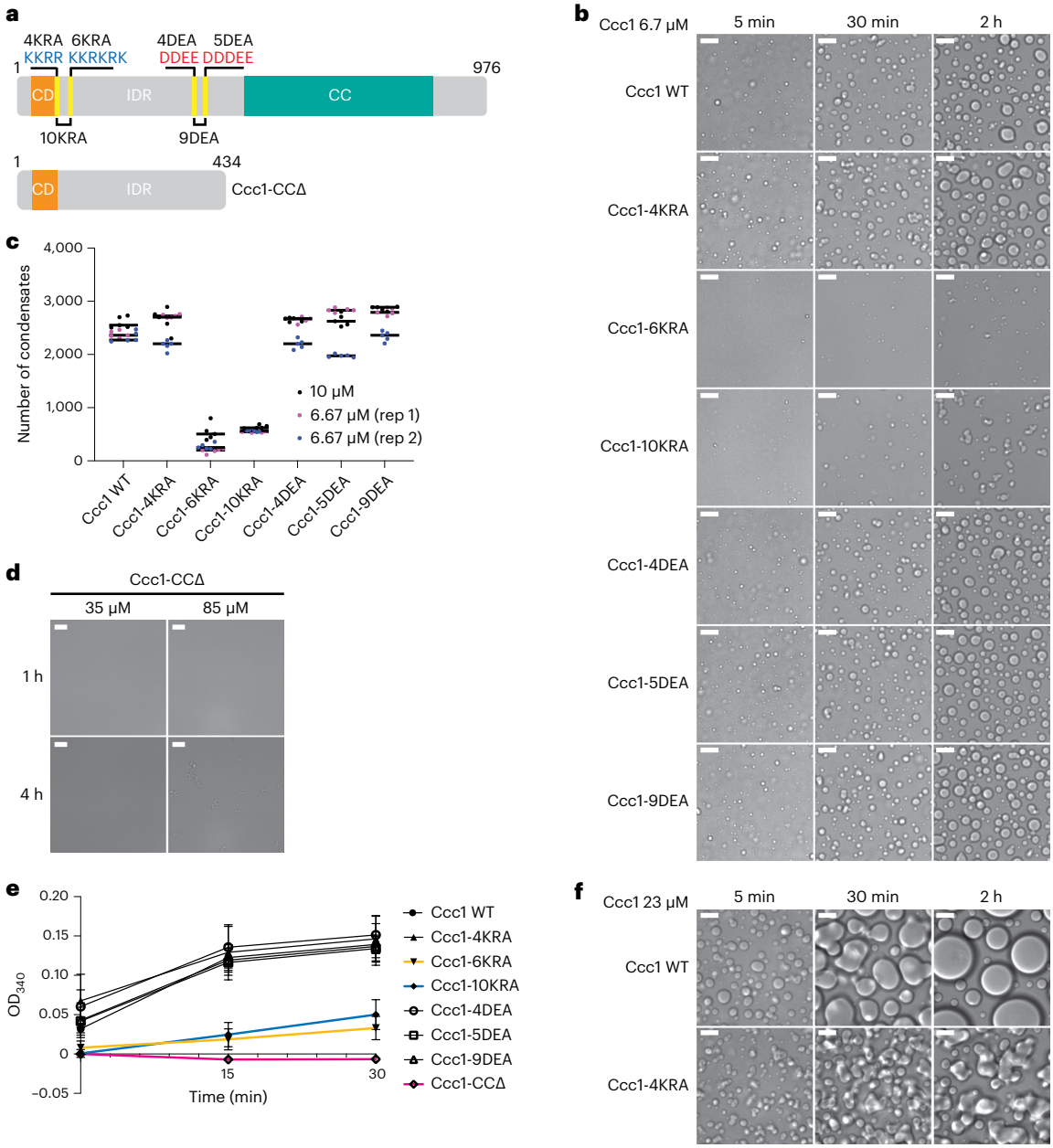

Fig. 2 | Phase separation is programmed by coiled-coil-mediated dimerization and two basic charged clusters in IDR. a, Schematic representation of Ccc1 IDR mutations and C-terminal truncation (Ccc1-CCΔ) to delete the coiled-coil. The positions of the six IDR mutations are as indicated. **b**, Condensation of 6.7 μM Ccc1 wild-type and mutants at indicated time points. Phase separation was induced at room temperature, 20 mM HEPES, pH 7.5 and 250 mM NaCl. Scale bars, 10 μm. **c**, Quantification of condensates of Ccc1 variants at 6.7 μM and 10 μM. Condensates formed after a 30-min induction were counted from five fields per strain. **d**, DIC images of Ccc1-CCΔ at 35 μM and 85 μM at indicated time points. Scale bars, 10 μm. **e**, Turbidity measurements of 2.8 μM Ccc1 wild-type and mutants at indicated time points (mean ± s.d., $n = 3$ independent replicates). **f**, DIC images of Ccc1 wild-type and 4KRA mutant at 23 μM at indicated time points. Scale bars, 10 μm. Data in **b**, **d** and **f** represent three independent experiments.

to the gel point, the greater the likelihood of generating gelation[26]. This is readily probed by querying condensate behaviors at higher protein concentrations. We compared the behaviors of Ccc1 wild-type and 4KRA at a higher concentration (23 μM) and found that the 4KRA condensates hardened to a more gel-like state (Fig. 2f and Supplementary Videos 1 and 2). In contrast to the wild-type protein, the 4KRA mutant formed irregular clumps that failed to become spherical. We propose that the altered material properties are due to higher densities of crosslinks introduced by the mutation, which decelerate molecular reconfigurations, leading to dynamically arrested phase separation[27,28].

Together, these in vitro studies indicate that two basic charge clusters in the IDR and the coiled-coil domain control the driving forces for phase separation of Ccc1. Importantly, these mutants allowed two qualitatively different types of phase separation perturbation—inhibition of phase separation (6KRA, 10KRA and Ccc1-CCΔ) and alteration of the material properties of the condensates (4KRA)—whereas mutation of the two acidic clusters had no detectable effect. We next tested the phenotypic effects of these mutants in vivo.

Phase separation-controlling elements program foci formation

To examine whether Ccc1 forms condensates in cells, we tagged chromosomal *CCC1* with a C-terminal codon-optimized 2xEGFP (enhanced GFP) by CRISPR (clustered regularly interspaced short palindromic repeats) editing[29,30] (Fig. 3a). By also tagging the nuclear pore protein

https://doi.org/10.1038/s41594-023-01000-z

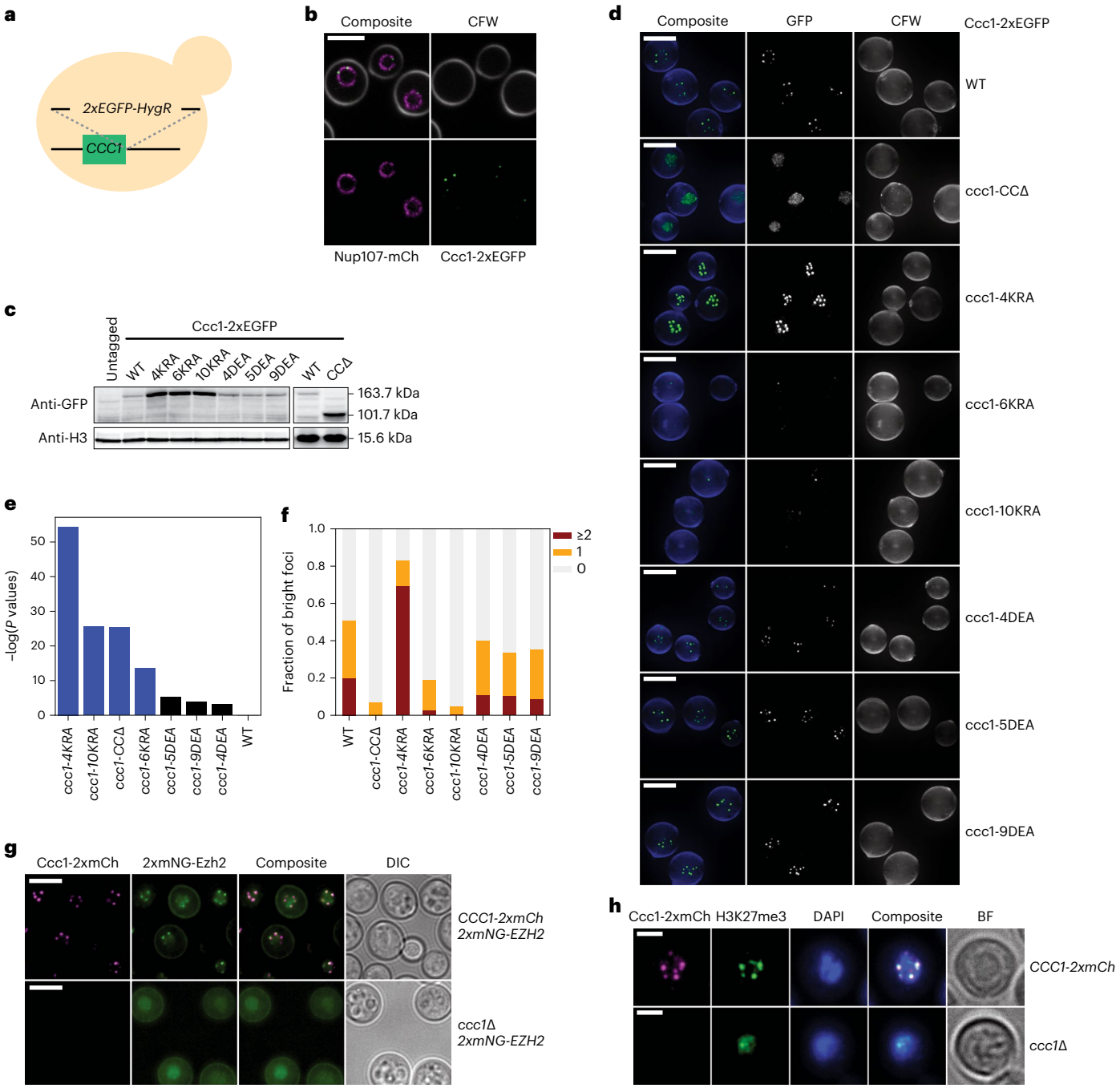

Fig. 3 | Phase separation-controlling elements program formation of nuclear condensation in vivo. a, Schematic representation of tagging chromosomal *CCC1* with 2xEGFP in *C. neoformans*. **b**, Confocal microscope images of cryptococcal cells expressing Ccc1-2xEGFP and Nup107-mCherry showing peripheral nuclear localization of Ccc1. Scale bar, 5 µm. **c**, Expression of Ccc1-2xEGFP in *CCC1* variant strains, as assessed by western blotting using the antibodies indicated on the left. H3 serves as a loading control. **d**, *Z*-projected with maximum intensity images of cryptococcal cells expressing C-terminally 2xEGFP-tagged Ccc1 wild-type and mutants. Scale bars, 5 µm. **e**, At least 180 cells per strain categorized by the number of bright foci per cell (0, 1 or ≥2). *P* values ($-\log_{10}$) are shown for a χ^2 test performed on contingency tables in which each mutant was compared with wild-type. **f**, Fraction of cryptococcal cells harboring 0, 1 or ≥2 bright foci per cell. **g**, Live cell images of cryptococcal cells expressing 2xmNeonGreen-Ezh2 (2xmNG) and Ccc1-2xmCherry (2xmCh) (top) and 2xmNG-Ezh2 in the absence of Ccc1 (bottom). Scale bars, 5 µm. **h**, Distribution of H3K27me3 in the cells indicated on the right. BF, brightfield. Scale bars, 2 µm. Data in **b**, **c**, **d**, **g** and **h** represent three independent experiments.

Nup107 (ref. 31) with a codon-optimized mCherry, we found that endogenous Ccc1 forms distinct foci at the nuclear periphery (Fig. 3b shows confocal slices), consistent with the association of telomeres with the nuclear envelope in eukaryotes[32].

To investigate whether the elements controlling phase separation in vitro also influence nuclear condensation of Ccc1, we generated cells expressing Ccc1 mutants tagged with C-terminal 2xEGFP at its own chromosomal locus. Western blotting showed expression of all mutants, with the basic cluster mutants and Ccc1-CCΔ displaying somewhat higher protein levels than wild-type (Fig. 3c). Exponentially growing live cells were examined by DeltaVision OMX super-resolution microscopy and *Z*-projected images (maximum intensity) were obtained (Fig. 3d).

The phenotypes of nuclear condensation in wild-type and mutants displayed a notably strong correlation with our in vitro data. First, the strain expressing 4KRA mutant (the 'hardening' mutant) formed more and brighter foci than wild-type. Cells expressing 6KRA and 10KRA, which displayed inhibited phase separation in vitro, rarely formed bright foci despite having higher protein levels than wild-type. The Ccc1-CCΔ protein, which was unable to phase separate in vitro, formed tiny speckles substantially smaller than wild-type nuclear foci, which were diffuse across the nucleus instead of forming a distinctive structure. Cells expressing the three acidic patch mutants did not show distinguishable phenotypes, also agreeing with the in vitro observations.

To quantify these effects, we developed a CellProfiler pipeline (Supplementary Table 1)[33]. We first normalized the intensity of each condensate to its area and then defined a 'bright' condensate as those in the top quartile of the intensity pool obtained from wild-type foci as a threshold. We categorized cells by the number of bright condensates per cell (0, 1 and ≥2; Fig. 3e,f). Whereas almost 70% of cells expressing the *ccc1-4KRA* allele had ≥2 bright foci per cell, the fraction of cells harboring bright foci decreased notably in *ccc1-6KRA*, *ccc1-10KRA* and *ccc1-CCΔ* mutants. By contrast, the three mutants in the acidic patches, which have no effect on phase separation in vitro, have no substantial effects on condensates in vivo. Our in vivo studies of wild-type and seven variants indicate that the determinants of phase separation of purified Ccc1 display markedly commensurate effects on endogenous Ccc1 condensates in cells. The simplest interpretation of these data is that Ccc1 forms condensates in cells via its propensity to undergo phase separation.

We investigated whether Ccc1 condensate formation contributes to anchoring PRC2 at the sites of action. We generated a strain expressing 2xmNeonGreen-Ezh2 and observed that it also forms foci. By additionally tagging *CCC1* with 2xmCherry, we assessed the relative localization of Ezh2 and Ccc1 at endogenous levels (Fig. 3g). Live cell imaging revealed a strong correlation of Ezh2 and Ccc1 foci, indicating that Ccc1 foci are enriched for PRC2. Whereas Ezh2 fails to form detectable foci in *ccc1Δ* (Fig. 3g), Ccc1 still forms foci in the absence of Ezh2 (Extended Data Fig. 5a), suggesting that Ccc1 condensates concentrate and anchor PRC2. This is further supported by our observation that Ezh2 is diffuse in the *ccc1* mutants defective in condensate formation (*ccc1-CCΔ*, *ccc1-6KRA* and *ccc1-10KRA*) (Extended Data Fig. 5b). In addition, we observed that Ccc1 colocalizes with H3K27me3 by performing immunofluorescence in the cells expressing Ccc1-2xmCherry (Fig. 3h and Extended Data Fig. 6a). The H3K27me3 signal appeared to be more dispersed within the nucleus in *ccc1Δ* cells as well as in *ccc1* mutants defective in condensate formation (Fig. 3h and Extended Data Fig. 6b). Together, these data are consistent with a model in which the partitioning of PRC2 into Ccc1 condensates is required for the proper deposition of the H3K27me3 mark. We next tested whether these mutants impacted the fidelity function of Ccc1.

Suppression of ectopic H3K27me3 requires Ccc1 phase separation

To avoid the potential functional negative impacts of the 2xEGFP tag, we precisely excised the corresponding sequences from the strains described above using CRISPR–Cas9 homology-directed repair[30] and then performed H3K27me3 chromatin immunoprecipitation with high-throughput sequencing (ChIP–seq) analysis (we acknowledge that the comparison to the microscopy phenotypes is limited by the distinct genotypes used). As described previously[15], we generated meta-centromere and meta-telomere plots to display the average centromeric and subtelomeric H3K27me3 enrichment signals, respectively (Fig. 4a,b and Extended Data Fig. 7a,b). With centromeres aligned at their midpoints and telomeres to the end of chromosomes, the average H3K27me3 signal is presented as a function of chromosomal position. We also measured the chromosomal background-subtracted read density of the H3K27me3 ChIP–seq signal at subtelomeric regions versus centromeres (Fig. 4c and Extended Data Fig. 7c). As we previously reported, *ezh2Δ* cells lost all H3K27me3 signals across the genome (Fig. 4c and Extended Data Fig. 7c,d). In *ccc1Δ* cells, centromeric H3K27me3 signal is increased whereas the H3K27me3 signal at the subtelomeric regions is reduced (Fig. 4a–c and Extended Data Fig. 7a–d), reproducing our previous findings[15].

H3K27me3 ChIP–seq analysis of *ccc1* mutants revealed that the elements controlling phase separation are also required for the proper deposition of H3K27me3 at subtelomeric locations. First, we found that the H3K27me3 enrichment pattern in the *ccc1-CCΔ* strain is remarkably similar to that of the *ccc1Δ* strain. The H3K27me3 signal is reduced at subtelomeres but increased at centromeres, indicating redistribution of Polycomb-mediated heterochromatin as in *ccc1Δ*. Together with the defective nuclear condensation phenotype of the *ccc1-CCΔ* mutant, this result suggests a functional role of Ccc1 coiled-coil in heterochromatin fidelity. Likewise, the three basic patch mutants also exhibited redistribution of H3K27me3 signal from subtelomeric domains to centromeres (Fig. 4a–c and Extended Data Fig. 7a–c). If bright condensate formation itself were important for heterochromatin fidelity, one would predict the *6KRA* and *10KRA* mutants to be defective in PRC2 anchoring and heterochromatin fidelity. Notably, the *4KRA* mutant, which appears to undergo dynamically arrested phase separation in vitro and forms brighter condensates in vivo, also showed a redistribution phenotype. This result demonstrates that the material properties of the Ccc1 condensates are also important for heterochromatin fidelity. Consistent with the redistribution of H3K27me3 observed above, the mutants harboring the Ccc1-KRA and Ccc1-CCΔ proteins displayed transcriptional derepression of subtelomeric genes (Fig. 4d). Also correlating with the in vitro and in vivo observations, the three mutants in the acidic clusters did not display significant changes.

Ccc1 condensates selectively concentrate PRC2 in vitro

The findings described above demonstrate that Ccc1 phase separation-controlling elements are required to suppress ectopic H3K27me3 deposition and strongly support a role of Ccc1 condensates in ensuring the fidelity of PRC2. Given that *C. neoformans* PRC2 subunits themselves contain IDRs (S.L. and H.D.M., unpublished), the simplest model would be that Ccc1 condensates directly sequester PRC2. To test this model, we investigated whether Ccc1 condensates could selectively concentrate PRC2 in vitro. For these studies and related structural biology studies, we cloned cDNA encoding *C. neoformans* Ezh2, Eed1, Bnd1 and Msl1, coexpressed them in insect cells and developed a scheme to purify the complex to apparent homogeneity (Extended Data Fig. 8a–c)[34]. The purified complex is catalytically active on a nucleosomal substrate (Extended Data Fig. 8d). Purified PRC2 and Ccc1 were each labeled with NHS (*N*-hydroxysuccinimide) ester-activated fluorescent dyes (DyLight 650 and 488) and mixed before inducing condensate formation through a salt shift (Fig. 5a). Although PRC2 (54 nM) alone did not drive phase separation under the conditions studied in the present article, the condensates formed by adding Ccc1 (5.4 μM) readily colocalized with the PRC2 signal, indicating that PRC2 rapidly partitioned into Ccc1 condensates (Fig. 5b,f). Concentrations of PRC2 and Ccc1 were based on the availability and the condition for forming spherical droplets.

Our previous work showed that redistribution of H3K27me3 to centromeres in *ccc1* chromodomain mutant is dependent on H3K9me2/3 (ref. 15). We also observed that HP1/Swi6 (yeast homolog of HP1) forms foci that are separated from Ccc1 foci in vivo (Supplementary Video 3 shows three-dimensional (3D) images of Swi6-2xmCherry and Ccc1-2xEGFP). Thus, we hypothesized that PRC2 may have a significant, albeit weaker, affinity to the phase-separated condensates of Swi6 (ref. 35), which would enable some recruitment to HP1 domains in the absence of sequestration by Ccc1. We expressed the 6xHis-tagged version of *C. neoformans* Swi6 in *E. coli* and purified it by affinity chromatography followed by size exclusion chromatography (Extended

https://doi.org/10.1038/s41594-023-01000-z

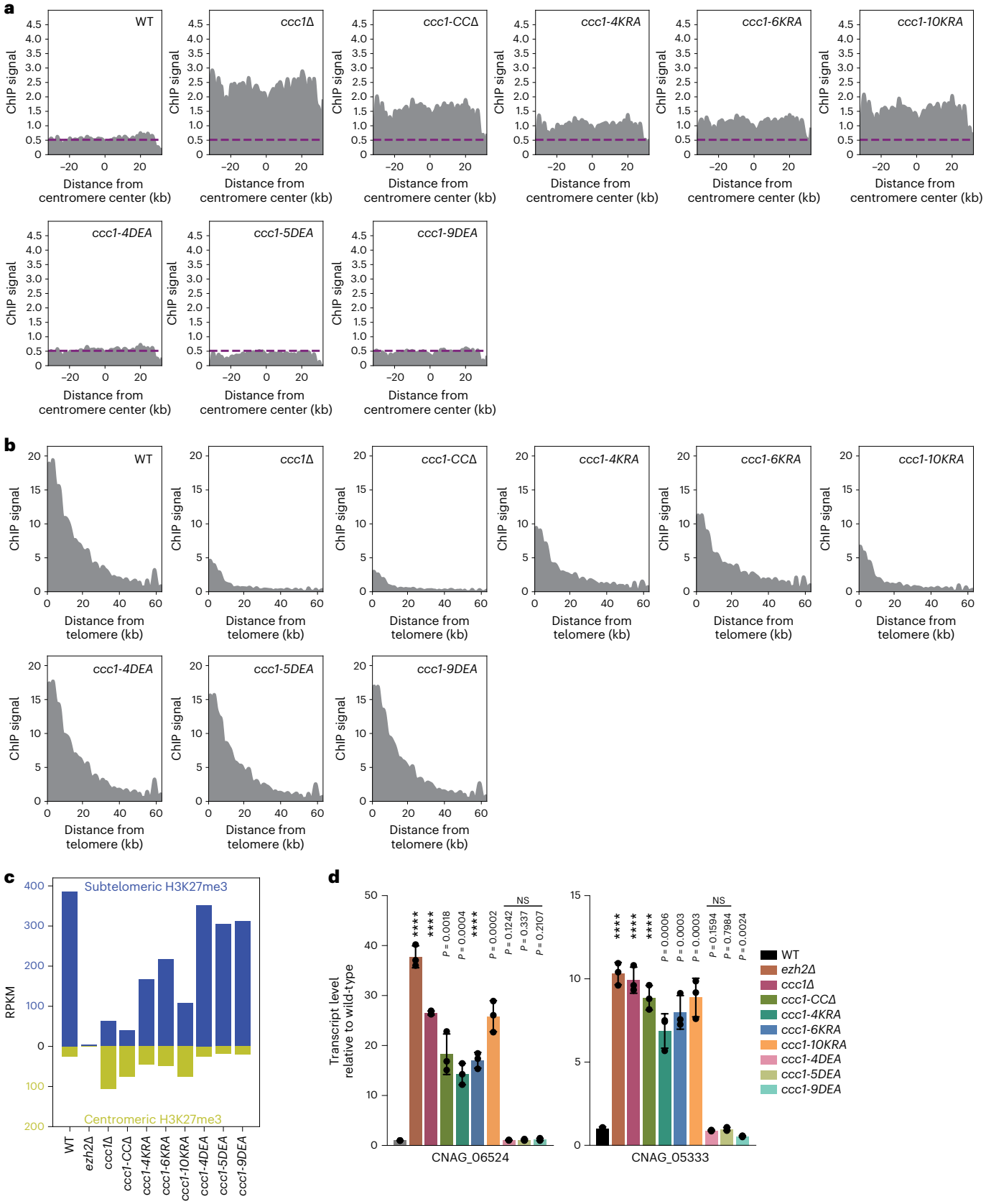

Fig. 4 | Suppression of ectopic H3K27me3 deposition by Ccc1 requires phase separation-controlling elements. a, Average centromeric H3K27me3, as measured by ChIP–seq. **b**, Average subtelomeric H3K27me3, as measured by ChIP–seq. **c**, H3K27me3 at subtelomeric versus centromeric regions as measured by ChIP–seq. Density (reads per kilobase per million mapped reads, RPKM) of signal above background is reported for subtelomeric (blue bar) and centromeric regions (green bar). **d**, Transcript levels of Ezh2 target genes in *CCC1* wild-type and mutant cells, as determined by quantitative reverse transcription PCR (RT–qPCR) (mean ± s.d., $n = 3$ independent replicates). Statistical significance between the wild-type and mutant determined by unpaired, two-tailed Student's *t*-test: ****$P < 0.0001$; NS, not significant.

https://doi.org/10.1038/s41594-023-01000-z

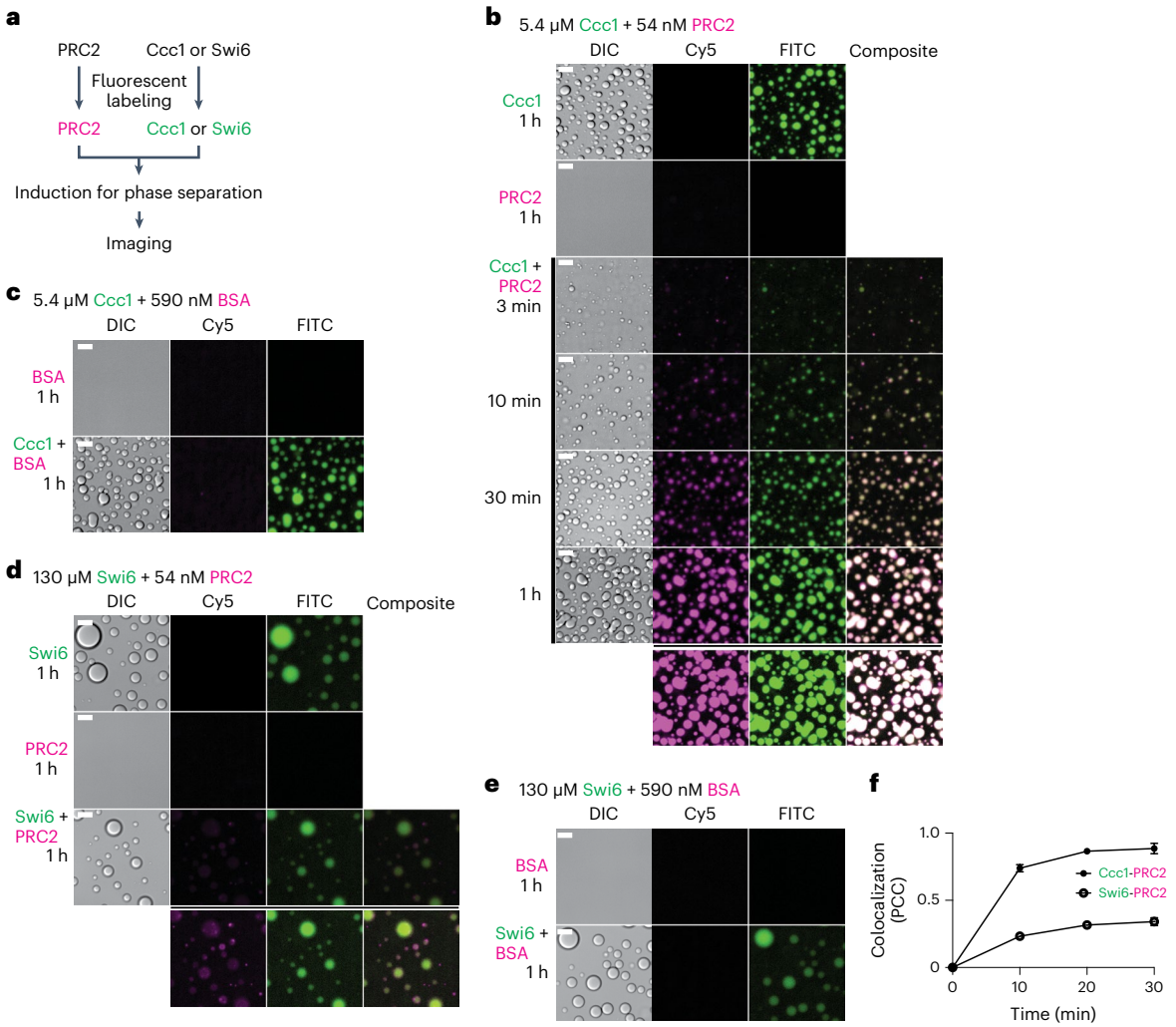

Fig. 5 | Ccc1 condensates selectively concentrate PRC2 in vitro. **a**, Recombinant PRC2 and Ccc1 or Swi6 fluorescently labeled using DyLight 650 (magenta) and DyLight 488 (green), respectively, and assembled before inducing phase separation. **b**, Ccc1 condensation in the presence of PRC2 at indicated time points. Bottom, images of Ccc1 with PRC2 at 1-h brightness adjusted as in **d**. **c**, Ccc1 condensation in the presence of fluorescently labeled BSA as a control. For **b** and **c**, condensation was induced at room temperature, 20 mM HEPES, pH 7.5 and 250 mM NaCl. **d**, Swi6 condensation in the presence of PRC2. Bottom, images of Swi6 with PRC2 at 1-h brightness adjusted. **e**, Swi6 condensation in the presence of fluorescently labeled BSA as a control. For **d** and **e**, condensation was induced at room temperature, 20 mM HEPES, pH 7.5 and 125 mM NaCl. Scale bars (**b**–**e**), 10 μm. **f**, Time course colocalization of PRC2 and Ccc1 or Swi6. The Pearson's correlation coefficient (PCC; mean ± s.d.) was measured from five fields per time point. Data in **b**, **c**, **d** and **e** represent two independent experiments.

Data Fig. 8e). Swi6 oligomerizes beyond a dimer (Extended Data Fig. 8f) and undergoes phase separation at a much higher concentration than Ccc1 (Extended Data Fig. 8g). We next tested whether PRC2 can be recruited to Swi6 condensates. Although Swi6 (130 μM) readily underwent phase separation, the partitioning of PRC2 into Swi6 condensates was considerably slower and weaker than its partitioning into Ccc1 condensates (Fig. 5d,f). This weak signal is indicative of specificity because a higher concentration of labeled bovine serum albumin (BSA; 590 nM) was not concentrated by either Ccc1 or Swi6 condensates (Fig. 5c,e). With the colocalization of Ezh2 and Ccc1 foci in live cells (Fig. 3g), these data demonstrate that PRC2 is selectively concentrated by Ccc1 condensates, supporting a potentially direct role for Ccc1 condensates in anchoring PRC2 in vivo. Due to the weak signals of Ezh2 and H3K27me3 in the *ccc1* mutants defective in condensate formation (Extended Data Figs. 5b and 6b), we were not able to visualize the redistribution of PRC2 in vivo by microscopy. Given the low ChIP signal of ectopic H3K27me3 at centromeres (Fig. 4a and Extended Data Fig. 7a), the degree of PRC2 redistribution is likely to be at or below the detection limit.

PRC2 displays low mobility within Ccc1 condensates

To further investigate the properties of Ccc1 and Swi6 condensates in vitro, we performed fluorescence recovery after photobleaching (FRAP) analysis. Swi6 displayed immediate recovery ($t_{½}$ = 0.9 s) as has been described for HP1α[36] (Fig. 6a,b). However, Ccc1 condensates did not show notable recovery over a 10-min time course, indicating considerably slower dynamics (Fig. 6c,d). Although both Ccc1 and Swi6 condensates undergo fusion, we observed that the Ccc1 condensates require minutes rather than seconds (Fig. 1g) to complete a fusion event and recover a spherical shape, whereas such events occurred virtually instantaneously with the Swi6 condensates (Extended Data Fig. 8h). These data indicate that the Ccc1 condensates have considerably lower mobility and distinctive viscoelastic properties compared with Swi6/HP1 condensates. To investigate the mobility of PRC2 in Ccc1 condensates, we performed FRAP experiments with Ccc1 condensates that had concentrated labeled PRC2 as described above. We observed that approximately 40% of the labeled PRC2 recovered its signal within 5 min ($t_{½}$ = 56 s for the mobile fraction) (Fig. 6e,f). These data indicate that the PRC2 concentrated within Ccc1 condensates is considerably more mobile than the condensate scaffold.

https://doi.org/10.1038/s41594-023-01000-z

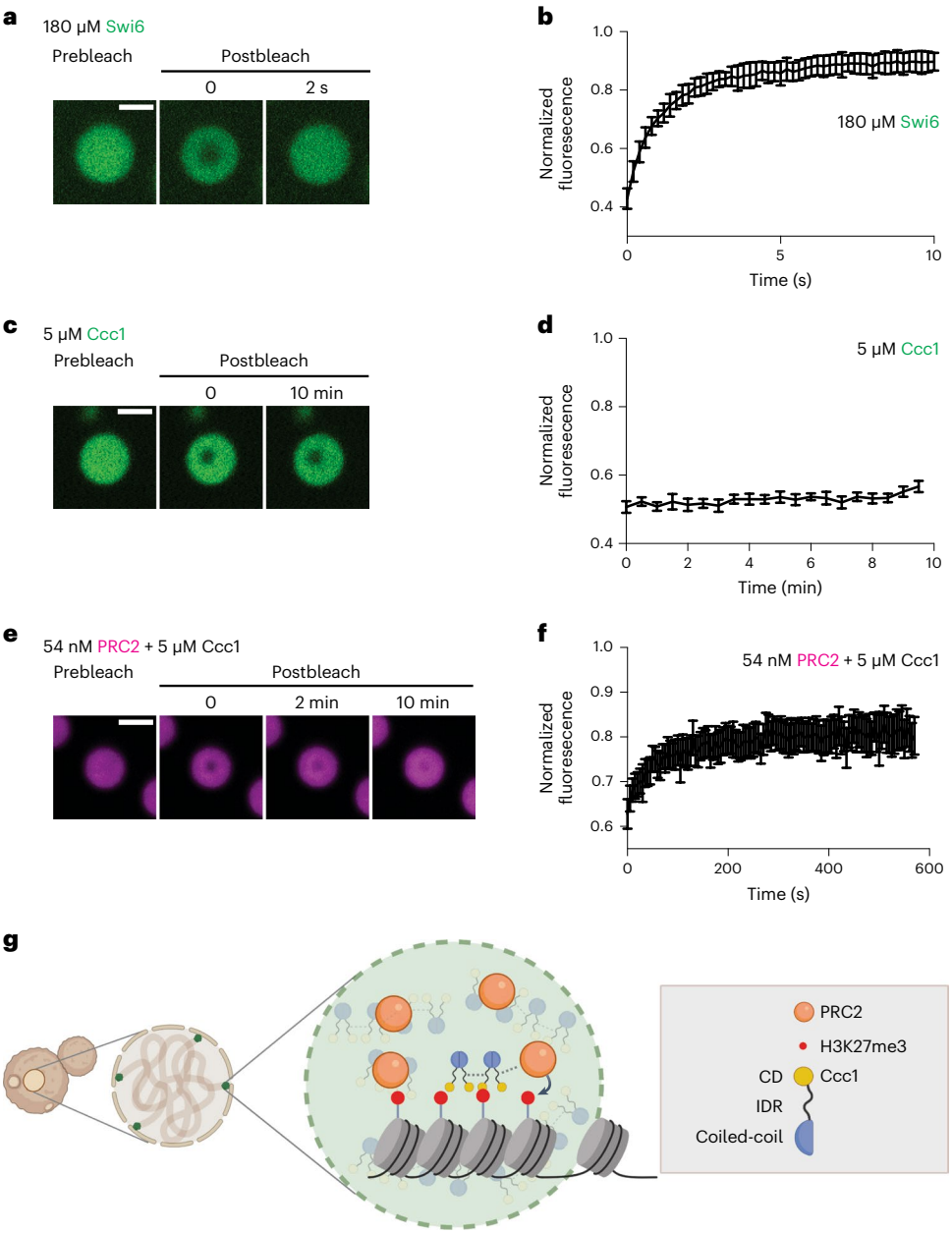

Fig. 6 | Ccc1 within droplets displays undetectable mobility whereas PRC2 displays low mobility. a, Snapshots of a fluorescently labeled Swi6 droplet analyzed by FRAP analysis. Scale bar, 2 μm. **b**, Quantitative analysis of the fluorescence recovery of Swi6 droplets (mean ± s.d., $n = 10$ independent experiments). **c**, Snapshots of a fluorescently labeled Ccc1 droplet analyzed by FRAP analysis. Scale bar, 2 μm. **d**, Quantitative analysis of the fluorescence recovery of Ccc1 droplets (mean ± s.d., $n = 10$ independent experiments). **e**, Snapshots of fluorescently labeled PRC2 partitioned into a Ccc1 droplet analyzed by FRAP analysis. Scale bar, 2 μm. **f**, Quantitative analysis of the fluorescence recovery of PRC2 within Ccc1 droplets (mean ± s.d., $n = 10$ independent experiments). **g**, A model for the role of Ccc1 condensates in promoting the fidelity of heterochromatin differentiation. Ccc1 is concentrated at subtelomeric domains via IDR–IDR interactions and dimerization through a coiled-coil, leading to condensate formation. By concentrating PRC2 within condensates, Ccc1 prevents erroneous recruitment of PRC2 and reinforces heterochromatin marks. CD, chromodomain. Fig. 6g created with BioRender.com.

Discussion

In previous work, we reported a conceptually new role for a chromatin reader protein, the Polycomb-like protein Ccc1, in promoting the fidelity of heterochromatin modification. In the absence of Ccc1 or when its chromodomain was mutated, we observed ectopic deposition of H3K27me3 at centromeric H3K9me3 domains[15]. We proposed an anchoring role for Ccc1, but in fact it was unclear how a conventional physical association with the PRC2 complex would achieve effective anchoring because dissociation from H3K27me3 domains would in principle allow modification elsewhere in the genome. Since reporting these observations, it has been shown that heterochromatin reader proteins and nucleosome arrays can undergo phase separation in vitro and HP1 has been found to display liquid-like behavior in vivo[3,4,7,8,35,36]. Phase separation can be promoted by associative interactions between disordered protein segments as well as more conventional interactions between folded domains[17,21,23]. IDR–IDR interactions can be mediated by opposite charges on side-chains, hydrophobic interactions and cation-π interactions. As Ccc1 harbors a large IDR with charge clusters, as well as a predicted coiled-coil domain, it appeared to be a protein with the potential multivalency required for phase separation. Indeed,

we found that recombinant Ccc1 phase separates readily in vitro in a manner that is antagonized by high salt. Ccc1 forms spherical droplets that fuse, but displays very slow dynamics, which suggests a more structured viscoelastic propensity relative to purely viscous systems. These in vitro properties raised the possibility that the biologically relevant anchoring/fidelity function of Ccc1 might be underpinned by its ability to form condensates.

We hypothesized that charged clusters in the IDR of Ccc1 and its coiled-coil domain might contribute to phase separation. Among the four most prominent clusters of like-charged residues in Ccc1, we identified two basic clusters that modulate phase separation, one that promotes it and another that limits condensate gel formation. In contrast, three mutations in two negatively charged clusters had no effect. Finally, the coiled-coil domain was essential for both phase separation and dimerization. Using precise gene replacement, we replaced the endogenous *CCC1* gene with these variants and tagged it with 2×EGFP. Super-resolution microscopy revealed a notable correlation with the in vitro phenotypes: wild-type Ccc1 formed foci. Whereas the mutants defective in phase separation (6KRA, 10KRA and CCΔ) formed considerably fewer foci, the 'gelling' mutant (4KRA) formed more and brighter foci. In contrast, the acidic cluster mutants (4DEA, 5DEA and 9DEA) displayed no detectable difference in phase separation or foci formation. These data strongly argue that the intrinsic associative properties of Ccc1 program its in vivo mesoscale behavior.

Given that Ccc1 foci are enriched for PRC2, we asked whether this behavior had any relevance to the biological function of Ccc1. We tested the effect of the mutants on H3K27me3 distribution in vivo. This analysis revealed that mutants that decrease the formation of bright foci (6KRA, 10KRA and CCΔ) or increase it (4KRA) display ectopic H3K27me3 deposition, whereas the three mutants that do not impact in vitro phase separation or in vivo focus formation display wild-type behavior. These findings lead us to conclude that the mesoscale properties of the Ccc1 protein are important for its biological function. The fidelity defect of the gelling 4KRA mutant, albeit modest, was not entirely expected because such a mutant might be anticipated to effectively anchor PRC2. A parsimonious model would be that the partitioning of a portion of newly synthesized PRC2 into 4KRA domains is defective in vivo.

The key questions we asked next were about: (1) how Ccc1 condensation could enable effective anchoring of the PRC2 complex in a manner that limits its access to HP1 heterochromatin and (2) how HP1 heterochromatin recruits it (albeit in a limited fashion) in the absence of Ccc1. To address these questions, we tested the simplest possibility, namely that Ccc1 condensates could directly and specifically concentrate PRC2. Indeed, this is precisely what we observed: Ccc1 droplets effectively concentrate an enzymatically active, recombinant four-subunit *C. neoformans* PRC2. By contrast, Swi6/HP1 droplets concentrate PRC2 only weakly, consistent with the significant but limited degree of ectopic H3K27me3 in cells lacking Ccc1. Consistent with the notion that Ccc1 functions to sequester a limiting amount of PRC2, we found that Ccc1 is considerably more abundant than PRC2 in cells (Extended Data Fig. 1a). We also showed that Ccc1 foci formation programmed by its IDR is required for concentrating PRC2 in vivo, raising the possibility that IDR–IDR interactions play a role in Ccc1 and PRC2 interaction (Fig. 6g). The mechanism of PRC2 concentration by Ccc1 condensates needs to be studied further.

Our results do not rule out additional roles for the phase separation propensities of heterochromatin reader proteins[9]. Indeed, the reduced H3K27me3 at subtelomeric regions in the condensate-altering Ccc1 mutants suggests that concentration of PRC2 by Ccc1 condensates may also be required for effective recruitment to its nucleosome substrate, its spread and/or its heritability. Conceptually, writer partitioning into a condensate offers a modified view of reader–writer coupling that superimposes phase separation on bimolecular binding reactions.

Our finding that Ccc1 associates with the HDAC ortholog Clr3 (Extended Data Fig. 1b), which is required for H3K27me3 (ref. 15), suggests that histone tail deacetylation may also play a role in these processes in vivo[37]. As histone tail deacetylation has been shown to promote phase separation of nucleosome arrays in vitro, cooperative action of reader and deacetylation-dependent nucleosome phase separation seems possible. Alternatively, deacetylation might primarily serve to enable tail modification by PRC2.

As outlined in the introduction, one of the human Polycomb paralogs, CBX2, a component of PRC1, harbors an IDR that mediates phase separation in vitro and focus formation in vivo[7,8]. Likewise, a component of the *Drosophila* PRC1 complex, Ph, has been shown to promote phase separation in vitro via the sterile α motif (SAM) domain interactions and a mutant defective in these interactions has been shown to have a phenotype in flies[38]. For CBX2, two mutants defective in phase separation and focus formation, one that alters 23 lysine residues and another that alters 13 lysine residues, have been shown to display axial patterning defects in mice[6,7]. As this region has been shown to mediate compaction of nucleosome arrays in vitro[5], it has been suggested that chromatin compaction may be the in vivo function of this region of CBX2 (ref. 7). However, the single molecular tracking experiments show low target site occupancy of PRC1 in live cells, which has been suggested to be inconsistent with a compaction function[39]. Moreover, artificial induction of Polycomb phase separation using heterologous multivalent interactions does not actively trigger compaction in vivo[40]. Thus, the function of animal PRC1 phase separation (and the ensuing Polycomb bodies) remains to be determined. To our knowledge, a role in heterochromatin fidelity akin to what we have described for Ccc1 has not been ruled out for these metazoan proteins.

Many chromatin-associated proteins and nucleosome arrays themselves have been shown to display a propensity to undergo phase separation in vitro[3,4,7,8,10,12,36,41,42]. In many cases, the same proteins are present in subnuclear foci in vivo. It has been stated that such properties may merely be an unavoidable consequence of the crowded intracellular environment and the physics of polymers rather than a reflection of biological significance[43,44]. In contrast to this view of 'condensates as side effects', the data in the present study provide evidence that the mesoscale biophysical properties of a chromatin reader protein are important for its in vivo function, one that requires the compartmentalization of chromatin-modifying enzyme at sites of its previous action. Such compartmentalization may be critical in a dense nuclear environment.

Online content

Any methods, additional references, Nature Portfolio reporting summaries, source data, extended data, supplementary information, acknowledgements, peer review information; details of author contributions and competing interests; and statements of data and code availability are available at https://doi.org/10.1038/s41594-023-01000-z.

References

1. Janssen, A., Colmenares, S. U. & Karpen, G. H. Heterochromatin: guardian of the genome. *Annu. Rev. Cell Dev. Biol.* **34**, 265–288 (2018).
2. Allshire, R. C. & Madhani, H. D. Ten principles of heterochromatin formation and function. *Nat. Rev. Mol. Cell Biol.* **19**, 229–244 (2018).
3. Larson, A. G. et al. Liquid droplet formation by HP1α suggests a role for phase separation in heterochromatin. *Nature* **547**, 236–240 (2017).
4. Strom, A. R. et al. Phase separation drives heterochromatin domain formation. *Nature* **547**, 241–245 (2017).
5. Grau, D. J. et al. Compaction of chromatin by diverse Polycomb group proteins requires localized regions of high charge. *Genes Dev.* **25**, 2210–2221 (2011).

6. Lau, M. S. et al. Mutation of a nucleosome compaction region disrupts Polycomb-mediated axial patterning. *Science* **355**, 1081–1084 (2017).
7. Plys, A. J. et al. Phase separation of Polycomb-repressive complex 1 is governed by a charged disordered region of CBX2. *Genes Dev.* **33**, 799–813 (2019).
8. Tatavosian, R. et al. Nuclear condensates of the Polycomb protein chromobox 2 (CBX2) assemble through phase separation. *J. Biol. Chem.* **294**, 1451–1463 (2019).
9. Kim, J. & Kingston, R. E. The CBX family of proteins in transcriptional repression and memory. *J. Biosci.* **45**, 16 (2020).
10. Gibson, B. A. et al. Organization of chromatin by intrinsic and regulated phase separation. *Cell* **179**, 470–484.e21 (2019).
11. Strickfaden, H. et al. Condensed chromatin behaves like a solid on the mesoscale in vitro and in living cells. *Cell* **183**, 1772–1784. e13 (2020).
12. Wang, L. et al. Histone modifications regulate chromatin compartmentalization by contributing to a phase separation mechanism. *Mol. Cell* **76**, 646–659.e6 (2019).
13. Narlikar, G. J. Phase-separation in chromatin organization. *J. Biosci.* **45**, 5 (2020).
14. Erdel, F. et al. Mouse heterochromatin adopts digital compaction states without showing hallmarks of HP1-driven liquid–liquid phase separation. *Mol. Cell* **78**, 236–249.e7 (2020).
15. Dumesic, P. A. et al. Product binding enforces the genomic specificity of a yeast polycomb repressive complex. *Cell* **160**, 204–218 (2015).
16. Hyman, A. A., Weber, C. A. & Jülicher, F. Liquid–liquid phase separation in biology. *Annu. Rev. Cell Dev. Biol.* **30**, 39–58 (2014).
17. Banani, S. F., Lee, H. O., Hyman, A. A. & Rosen, M. K. Biomolecular condensates: organizers of cellular biochemistry. *Nat. Rev. Mol. Cell Biol.* **18**, 285–298 (2017).
18. Alberti, S., Gladfelter, A. & Mittag, T. Considerations and challenges in studying liquid–liquid phase separation and biomolecular condensates. *Cell* **176**, 419–434 (2019).
19. Patel, S. S., Belmont, B. J., Sante, J. M. & Rexach, M. F. Natively unfolded nucleoporins gate protein diffusion across the nuclear pore complex. *Cell* **129**, 83–96 (2007).
20. Zhang, Q. et al. Visualizing dynamics of cell signaling in vivo with a phase separation-based kinase reporter. *Mol. Cell* **69**, 334–346. e4 (2018).
21. Qamar, S. et al. FUS phase separation is modulated by a molecular chaperone and methylation of arginine cation-π interactions. *Cell* **173**, 720–734.e15 (2018).
22. Wang, J. et al. A molecular grammar governing the driving forces for phase separation of prion-like RNA binding proteins. *Cell* **174**, 688–699.e16 (2018).
23. Simon, J. R., Carroll, N. J., Rubinstein, M., Chilkoti, A. & López, G. P. Programming molecular self-assembly of intrinsically disordered proteins containing sequences of low complexity. *Nat. Chem.* **9**, 509–515 (2017).
24. Choi, J.-M., Holehouse, A. S. & Pappu, R. V. Physical principles underlying the complex biology of intracellular phase transitions. *Annu. Rev. Biophys.* **49**, 107–133 (2020).
25. Brangwynne, C. P., Tompa, P. & Pappu, R. V. Polymer physics of intracellular phase transitions. *Nat. Phys.* **11**, 899–904 (2015).
26. Harmon, T. S., Holehouse, A. S., Rosen, M. K. & Pappu, R. V. Intrinsically disordered linkers determine the interplay between phase separation and gelation in multivalent proteins. *eLife* **6**, e30294 (2017).
27. Ranganathan, S. & Shakhnovich, E. I. Dynamic metastable long-living droplets formed by sticker-spacer proteins. *eLife* **9**, e56159 (2020).
28. Boeynaems, S. et al. Spontaneous driving forces give rise to protein–RNA condensates with coexisting phases and complex material properties. *Proc. Natl Acad. Sci. USA* **116**, 7889–7898 (2019).
29. Fan, Y. & Lin, X. Multiple applications of a transient CRISPR–Cas9 coupled with electroporation (TRACE) system in the *Cryptococcus neoformans* species complex. *Genetics* **208**, 1357–1372 (2018).
30. Huang, M. Y. et al. Short homology-directed repair using optimized Cas9 in the pathogen *Cryptococcus neoformans* enables rapid gene deletion and tagging. *Genetics* **220**, iyab180 (2022).
31. Walther, T. C. et al. The conserved Nup107–160 complex Is critical for nuclear pore complex assembly. *Cell* **113**, 195–206 (2003).
32. Ebrahimi, H. & Cooper, J. P. Finding a place in the SUN: telomere maintenance in a diverse nuclear landscape. *Curr. Opin. Cell Biol.* **40**, 145–152 (2016).
33. McQuin, C. et al. CellProfiler 3.0: next-generation image processing for biology. *PLoS Biol.* **16**, e2005970 (2018).
34. Weissmann, F. et al. biGBac enables rapid gene assembly for the expression of large multisubunit protein complexes. *Proc. Natl Acad. Sci. USA* **113**, E2564–E2569 (2016).
35. Sanulli, S. et al. HP1 reshapes nucleosome core to promote phase separation of heterochromatin. *Nature* **575**, 390–394 (2019).
36. Keenen, M. M. et al. HP1 proteins compact DNA into mechanically and positionally stable phase separated domains. *eLife* **10**, e64563 (2021).
37. Fan, H. et al. BAHCC1 binds H3K27me3 via a conserved BAH module to mediate gene silencing and oncogenesis. *Nat. Genet.* **52**, 1384–1396 (2020).
38. Seif, E. et al. Phase separation by the polyhomeotic sterile alpha motif compartmentalizes Polycomb group proteins and enhances their activity. *Nat. Commun.* **11**, 5609 (2020).
39. Huseyin, M. K. & Klose, R. J. Live-cell single particle tracking of PRC1 reveals a highly dynamic system with low target site occupancy. *Nat. Commun.* **12**, 887 (2021).
40. Eeftens, J. M., Kapoor, M., Michieletto, D. & Brangwynne, C. P. Polycomb condensates can promote epigenetic marks but are not required for sustained chromatin compaction. *Nat. Commun.* **12**, 5888 (2021).
41. Grau, D. et al. Structures of monomeric and dimeric PRC2:EZH1 reveal flexible modules involved in chromatin compaction. *Nat. Commun.* **12**, 714 (2021).
42. Zhang, Y. et al. Nuclear condensates of p300 formed though the structured catalytic core can act as a storage pool of p300 with reduced HAT activity. *Nat. Commun.* **12**, 4618 (2021).
43. Darzacq, X. & Tjian, R. Weak multivalent biomolecular interactions: a strength versus numbers tug of war with implications for phase partitioning. *RNA* **28**, 48–51 (2022).
44. McSwiggen, D. T., Mir, M., Darzacq, X. & Tjian, R. Evaluating phase separation in live cells: diagnosis, caveats, and functional consequences. *Genes Dev.* **33**, 1619–1634 (2019).

Methods

Yeast strains and growth conditions

Yeast strains used in the present study are listed in Supplementary Table 2. *C. neoformans* strains were constructed by biolistic transformation[45] or CRISPR-based homologous recombination[29,30]. Sequences of oligonucleotides are listed in Supplementary Table 3. Genetic manipulations were confirmed by PCR and Sanger sequencing. *C. neoformans* strains were grown in YPAD medium at 30 °C.

Affinity purification and mass spectrometry

C. neoformans strains encoding CBP-2xFlag-tagged Ezh2 and Ccc1 were grown to log phase, harvested and snap frozen. Frozen cells were pulverized in a Freezer/Mill (SPEX SamplePrep 6870) and thawed lysates were treated with 1,000 U of RQ1 DNase (Promega, catalog no. M6101) for 30 min at room temperature. Once the lysates were cleared by centrifugation at 40,000*g* for 40 min at 4 °C, tagged proteins were purified using anti-Flag M2 Affinity Gel (Sigma-Aldrich, catalog no. A2220) and eluted with 3xFLAG peptide (Sigma-Aldrich, catalog no. F4799). Flag eluates were purified using Calmodulin Affinity Resin (Agilent, catalog no. 214303) and then eluted using 3 mM ethylene glycol bis(2-aminoethyl) tetraacetic acid (EGTA). Purified proteins and associating partners were analyzed by mass spectrometry as previously described[15,46].

Analysis of protein disorder, structure and charge distribution

Prediction of protein disorder and structured domains was performed using IUPred3 (ref. 47), InterProScan5 (ref. 48), Waggawagga[49] and Multicoil2 (ref. 50). The charge distribution of Ccc1 was calculated using CIDER[51].

Recombinant protein expression and purification

The cDNAs of Ccc1 wild-type, mutants and Swi6 were cloned into a pBH4 vector for expression and purified from *E. coli* BL21 (DE3) strains. Cells were grown to an optical density at 600 nm (OD_{600}) 0.6–0.8 at 37 °C in 2× Luria-Bertani (LB) broth with 100 μg ml^{-1} of carbenicillin and induced with 0.1 mM isopropyl β-D-1-thiogalactopyranoside (IPTG) at 18 °C for 18 h. Cell pellets were resuspended in lysis buffer (20 mM HEPES, pH 7.5, 300 mM NaCl, 10 mM imidazole and 10 % (v:v) glycerol) with 10 mM phenylmethylsulfonyl fluoride (PMSF) and protease inhibitors (Sigma-Aldrich, catalog no. P8849) and lysed by sonication (Qsonica 5). Cell lysate was cleared by centrifugation at 20,000*g* for 30 min at 4 °C and incubated with HisPur Cobalt resin (Thermo Fisher Scientific, catalog no. 89964) for 1 h at 4 °C. Resin was washed with 20 resin-bed volumes of lysis buffer and eluted with elution buffer (20 mM HEPES, pH 7.5, 300 mM NaCl, 250 mM imidazole and 10% (v:v) glycerol). For full-length Ccc1, eluate was dialyzed into HiTrap butyl buffer A (50 mM sodium phosphate, pH 7.2, 0.5 M ammonium sulfate and 10% (v:v) glycerol) and injected on a HiTrap butyl HP column (GE Healthcare, catalog no. 28411005). Elution was performed with a 0–100% linear gradient of HiTrap butyl buffer B (50 mM sodium phosphate, pH 7.2 and 10% glycerol) over 10 column volumes. Alternatively, affinity-purified protein was injected on a HiLoad 16/600 Superose 6 pg SEC column (GE Healthcare, catalog no. 29323952) to run with storage buffer (20 mM HEPES, pH 7.5, 500 mM NaCl, 1 mM dithiothreitol (DTT) and 10% (v:v) glycerol). Hydrophobic interaction chromatography and size exclusion chromatography achieved a comparable level of protein purity. For Ccc1-CCΔ and Swi6, size exclusion chromatography was performed on a HiLoad 16/600 Superose 6 pg SEC column with storage buffer (20 mM HEPES, pH 7.5, 250 mM NaCl, 1 mM DTT and 10% (v:v) glycerol). Purified proteins were concentrated using Amicon Ultra Centrifugal Filter units (EMD Millipore, catalog no. UFC905024) and snap frozen in liquid N_2 to store at −70 °C.

Mass photometry analysis

Mass photometry measurements were carried out on a Refeyn OneMP mass photometer; 15 μl of buffer (20 mM HEPES, pH 7.5, and 250 mM NaCl) was loaded within silicone gaskets (Grace Bio-Labs) on a cleaned cover glass slide. Once signal and focus were optimized, 1 μl of protein was added to the buffer and mixed well by pipetting to achieve a final protein concentration of 50–75 nM. Images were acquired for 60 s (5,880 frames) and analyzed using DiscoverMP (Refeyn). BSA (monomer, 66 kDa, and dimer, 132 kDa) and apoferritin (24-mer, 480 kDa) were used for calibration.

Turbidity measurement of protein condensates

Purified Ccc1 was buffer exchanged to 20 mM HEPES, pH 7.5, and 500 mM NaCl to get rid of DTT and glycerol in storage buffer. Phase separation was induced by adding 1 volume of 20 mM HEPES, pH 7.5 to achieve a final concentration of 250 mM NaCl. Proteins, 15 μl, were immediately loaded into a clear-bottomed 384-well plate (Corning). Absorbance ($A_{340\,nm}$) was measured using a Synergy H1 plate reader (BioTek) at room temperature and analyzed by GraphPad Prism 9.

Microscope imaging of protein condensates

Proteins were buffer exchanged to 20 mM HEPES, pH 7.5, and 500 mM NaCl and diluted to a concentration to be tested. Once phase separation had been induced, 15 μl of proteins was immediately plated on to a glass-bottomed, 384-well plate (Greiner Bio-One) and imaged on a Nikon Ti2 Eclipse inverted epifluorescence microscope with a ×40 objective at room temperature. Counting protein condensates in a field at a 30-min timepoint was performed by Find Maxima algorithm in Fiji and the data were analyzed by GraphPad Prism 9. Labeled proteins were imaged using FITC and Cy5 filter sets and a ×40 objective. Images were analyzed in Fiji and the data were analyzed by GraphPad Prism 9.

Protein labeling

Purified Ccc1 and Swi6 were labeled using an amine-reactive dye, DyLight 488 NHS Ester (Thermo Scientific, catalog no. 46403). Approximately 250–500 μl of purified protein at 1 mg ml^{-1} was added to the vial containing the dye, mixed well by brief vortexing and incubated for 1 h at room temperature. Nonreactive dyes were removed using dye removal columns (Thermo Fisher Scientific, catalog no. 22858) or by dialysis. Labeled and unlabeled proteins were mixed (1:25–1:50) before inducing phase separation. Recombinant PRC2 was labeled with DyLight 650 NHS Ester (Thermo Fisher Scientific, catalog no. 62266).

Live cell imaging

To examine localization of Ccc1, *C. neoformans* cells encoding both C-terminal 2×EGFP-tagged Ccc1 and C-terminal mCherry-tagged Nup107 were grown in synthetic complete medium at 30 °C to log phase. For cell wall staining, cells were harvested, washed with phosphate-buffered saline (PBS) and resuspended in 50 μl of PBS containing Calcofluor white (20 μg ml^{-1}; Sigma-Aldrich, catalog no. F3543). After a 5-min incubation, cells were washed with PBS twice. Live cell imaging was done on a Nikon Ti-inverted fluorescence microscope with CSU-22 spinning disk confocal using DAPI, FITC and Cy3 filter sets and a ×100 oil objective. Images were analyzed in Fiji.

To quantify nuclear condensation, *C. neoformans* cells encoding C-terminally 2×EGFP-tagged Ccc1 wild-type and mutants were grown in YPAD at 30 °C to log phase, harvested and stained with Calcofluor white. Live cell imaging was carried out on a DeltaVision OMX Super Resolution microscopy system using DAPI and 488-nm channels. A Z-stack of images was acquired with 0.125-μm spacing and projected using maximum intensity. Images were analyzed with CellProfiler using a customized pipeline[33] (Supplementary Table 1). In brief, cell membranes and foci, along with measurements of brightness and area, were identified. Foci contained within a cell membrane were retained and all others were filtered out. Brightness of foci was normalized to the respective area. Bright foci were defined as ones with a value above the upper 75% quantile of the wild-type.

To investigate colocalization of Ezh2 and Ccc1, live cells expressing both 2xmNeonGreen-Ezh2 and Ccc1-2xmCherry (wild-type and mutants) were grown in YPAD at 30 °C to log phase, washed with PBS and imaged on a Nikon Eclipse Ti2-inverted fluorescence microscope with a ×100 oil objective. Images were analyzed in Fiji.

Immunofluorescence

Immunofluorescence to detect H3K27me3 was performed in *C. neoformans* cells expressing Ccc1-2xmCherry. Cells were grown in 20 ml of YPAD at 30 °C to OD_{600} of 0.5, harvested and washed with water. Cells were treated with lysing enzymes from *Trichoderma harzianum* (10 mg ml^{-1}, Sigma-Aldrich, catalog no. L1412) in 5 ml of spheroplast buffer (100 mM sodium citrate, pH 6.0, 1 M sorbitol, 10 mM EDTA and 35 mM 2-mercaptoethanol) for 2 h at 37 °C. Digested cells were fixed in ice-cold methanol for 30 min at −20 °C, washed with PBS 3× and permeabilized in PBS containing 1% (v:v) Triton X-100 (PBST) for 10 min at room temperature. Cells were then washed with PBS and treated with blocking buffer (0.1% PBST containing 1% BSA) for 1 h. Cells were incubated with the antibody against H3K27me3 (1:100 diluted in blocking buffer) overnight at 4 °C, washed with blocking buffer and treated with Alexa Fluor-488 goat anti-rabbit IgG H&L (1:1,000 diluted in blocking buffer; Abcam, catalog no. ab150085) in the dark for 1 h at room temperature. Next, cells were washed with blocking buffer, counterstained with DAPI (5 µg ml^{-1} in PBS) for 30 min in the dark and washed with PBS. Imaging was performed on a DeltaVision OMX Super Resolution microscopy system. Images were analyzed in Fiji.

Western blotting

C. neoformans cells were cultured in YPAD medium at 30 °C and harvested at OD_{600} of 1.0. Cell pellets were resuspended in 200 µl of 10% trichloroacetic acid. After a 10-min incubation on ice, pellets were centrifuged at 12,500*g* for 5 min at 4 °C and washed with ice-cold acetone. Air dried pellets were resuspended in 200 µl of 2× Laemmli buffer adjusted with 80 µl of Tris-HCl, pH 8.0 and bead-beaten 2× for 90 s. The lysates were boiled at 100 °C for 5 min and centrifuged at 20,000*g* for 10 min. The supernatant was collected and resolved on 4–12% NuPAGE Bis-Tris protein gels (Invitrogen). Gels were transferred on to nitrocellulose membranes at 30 V for 2 h. Membranes were blocked for 1 h in 5% (w:v) milk in tris-buffered saline and Tween-20 (TBST) and washed with TBST for 3 × 5 min. Western blotting was performed with rabbit polyclonal anti-GFP (1:3,000, Abcam, catalog no. ab290 or 1:3,000, Invitrogen, catalog no. A11122) and rabbit polyclonal histone H3 antibody (1:1,000, Invitrogen, catalog no. PA5-16183) diluted with 5% milk in TBST for 1 h followed by four 5-min washes in TBST. The membranes were then incubated with horseradish peroxidase-conjugated, secondary antibody goat anti-rabbit (1:20,000; BioRad, catalog no. 1706515) for 1 h followed by four 5-min washes in TBST. Membranes were developed using a SuperSignal West Femto Maximum Sensitivity Substrate kit (Thermo Fisher Scientific, catalog no. 34095) and imaged using an Azure imager.

ChIP

ChIP was performed as previously described[15] with modifications. *C. neoformans* cells at OD_{600} of 1.0 were crosslinked with formaldehyde and lysed using a bead beater (Omni International, 8× for 90 s). Lysates were clarified by centrifugation at 6,800*g* for 10 min and the pellet was sonicated using a Bioruptor Pico (Diagenode, 25 cycles of 30 s on and 30 s off). The supernatant collected by centrifugation at 20,000*g* for 20 min was incubated with antibody against H3K27me3 and protein A Dynabeads (Invitrogen, catalog no. 10002D) overnight at 4 °C. Library preparation was carried out using NEBNext Ultra II DNA Library Prep Kit (New England BioLabs, catalog no. E7103L).

ChIP–seq analysis

Sequencing reads were trimmed for adapter sequence (GATCGGAAGA) using Cutadapt[52] and aligned to the *C. neoformans* genome using Bowtie (modified parameters: -v2, -M1, --best)[53]. Alignment files were sorted and indexed using SAMtools[54] and bedgraph files were generated using BEDTools[55]. Each bedgraph file was scaled by a million aligned reads, normalized to the corresponding whole-cell extract at each genomic position and smoothed using a 500-bp centered rolling mean. For meta-centromere and meta-telomere plots, bedgraph read depth values were summed using 'bedtools map -o sum' against customized defined, 1,000-bp bins spanning each telomere or centromere, as well as against noncentromeric and nontelomeric loci. A background read depth value was determined as the total noncentromeric and nontelomeric bedgraph values per chromosome divided by the total length of noncentromeric and nontelomeric DNA on each given chromosome. For each 1,000-bp bin, the total read depth sum was divided by the bin width and the background value for the matched chromosome was subtracted from this value to yield an average read depth value for that bin. The reported values in the figures reflect the average value of the *n*th bin across all *n*th bins on all chromosomes. For read-density plots, centromeric reads, telomeric reads, background (noncentromeric and nontelomeric) reads, as well as total reads were counted from bam files using 'samtools view –L'. Reads per kilobase per million mapped reads (RPKM) values were calculated as (reads per feature × 1000,000,000)/(length of feature × total reads in sample). Reported log(fold-change) values were calculated as $\log_{10}$(telomeric or centromeric RPKM/background RPKM).

RT–qPCR

C. neoformans cells were cultured in YPAD medium at 30 °C and harvested at an OD_{600} of 1.0. Cell pellets were resuspended in 0.5 ml of TRIzol (Thermo Fisher Scientific, catalog no. 15596026) with 0.5-mm Zirconia/Silica Beads (BioSpec Products, catalog no. 11079105Z) and lysed using a bead beater for 1 min. Chloroform, 100 µl (Sigma-Aldrich, catalog no. 472476) was added and mixed gently and then centrifuged at 12,500*g* for 15 min at 4 °C. The upper aqueous phase was collected and further purified using an RNA clean and concentrator kit (Zymo Research, catalog no. R1013). Reverse transcription (RT) was performed on 1 µg of DNase-treated RNA using a SuperScript III Reverse Transcriptase (Invitrogen, catalog no. 18080044). Quantitative PCR was performed using a PowerUP SYBR Green Master Mix (Applied Biosystems, catalog no. A25742) to determine the expression of CNAG_06524 and CNAG_05333 relative to *ACT1* and the data were analyzed by GraphPad Prism 9.

Expression and purification of recombinant PRC2

The cDNAs of four components of the PRC2 complex (EZH2, EED1, BND1 and MSL1) were cloned into a pLIB vector individually to generate a gene expression cassette (GEC) containing a polyhedrin promoter, a tagged cDNA and an SV40 terminator. Each cDNA was tagged as follows: pLIB-3xStrep-TagII-HRV3C-EZH2, pLIB-9xHis-HRV3C-EED1, pLIB-Flag-HRV3C-BND1 and pLIB-6xHis-TEV-MSL1. Four GECs were amplified and cloned together into a pBIG1a baculovirus expression plasmid by Gibson assembly[34]. Bacmid containing the complex was generated in DH10Bac cells and used for infection and expression in SF9 insect cells for 72 h at 27 °C. After expression, cell pellets were lysed using an Emulsiflex C3 homogenizer (Avestin) in purification buffer containing 20 mM HEPES, pH 7.5, 0.5 mM $MgCl_2$, 20% glycerol, 1 mM DTT and 600 mM NaCl with protease inhibitor mix (Roche). Clarified lysate was incubated with Anti-Flag M2 Affinity Gel (Sigma-Aldrich) for 2 h. The beads were washed extensively with the purification buffer. The complex was eluted off the beads using 4 mg of Flag peptides (Bio-Synthesis Inc.) and dialyzed into HiTrapQ buffer A (20 mM Tris-HCl, pH 7.5, 150 mM NaCl and 1 mM DTT). The complex was bound

to a HiTrap Q FF column (GE Healthcare) and eluted with a linear gradient of HiTrapQ buffer B (20 mM Tris-HCl, pH 7.5, 1 M NaCl and 1 mM DTT). The peak fraction containing the four-component complex was then applied to a Superose 6 Increase column (GE Healthcare) pre-equilibrated with the storage buffer (20 mM HEPES, pH 7.9, 50 mM NaCl, 5% glycerol and 2 mM 2-mercaptoethanol). Peak fractions containing the four-component PRC2 complex were concentrated, snap frozen and stored at −80 °C.

Histone methyltransferase assay

Methyltransferase activity of the recombinant PRC2 on nucleosome assembled with H3 (*Xenopus* histone H3 with 28SAPAT32 that was replaced for 28QTTTSAA34 of *C. neoformans* histone H3). Reaction volumes of 20 µl containing PRC2 were mixed with 300 nM nucleosomes in methyltransferase buffer (20 mM Tris-HCl, pH 8.0, 50 mM NaCl, 1 mM DTT, 0.1 mg ml^{-1} of BSA and 40 µM *S*-adenosyl methionine). The reactions were incubated for 30 min at 30 °C and stopped with 5 µl of 0.5% trifluoroacetic acid. The *S*-adenosyl-L-homocysteine produced was measured using MTase-Glo Methyltransferase Assay Kit (Promega, catalog no. V7601). Luminescence measurements were performed using an EnSpire 2300 Multilabel plate reader (Perkin Elmer) and the data were analyzed by GraphPad Prism 9.

FRAP analysis

FRAP experiments were performed on a Nikon Ti-inverted fluorescence microscope with CSU-W1 confocal using a ×100/1.4 numerical aperture oil immersion objective at room temperature. Condensates were assembled in 10 µl as follows: 5 µM Ccc1 containing 2% labeled Ccc1 in 20 mM HEPES, pH 7.5, 250 mM NaCl, 180 µM Swi6 containing 2% labeled Swi6 in 20 mM HEPES, pH 7.5, 125 mM NaCl, and 5 µM Ccc1 with 54 nM labeled PRC2 in 20 mM HEPES, pH 7.5 and 250 mM NaCl. FRAP experiments were done within 1 h of proteins being plated on to a glass-bottomed, 384-well plate (Greiner Bio-One). Ccc1 photobleaching was done with a 405-nm laser for 100-ms exposure at 30 mW of laser power. Postbleaching images were acquired with a 1-min interval for 10 min. Swi6 photobleaching was done with a 405-nm laser for 1-s exposure at 100 mW of laser power. Postbleaching images were acquired with a 200-ms interval for 10 s. Photobleaching of PRC2 was performed with a 405-nm laser for 300-ms exposure at 30 mW of laser power. Postbleaching images were acquired with a 5-s interval for 10 min. Intensity measurements were done with Fiji and the data were analyzed by GraphPad Prism 9. Fluorescence intensities of photobleached regions were corrected by unbleached control regions and then normalized to prebleached intensities[56].

Reporting summary

Further information on research design is available in the Nature Portfolio Reporting Summary linked to this article.

Data availability

ChIP–seq data were deposited in the Gene Expression Omnibus under accession no. GSE195824. Live cell imaging data to quantify nuclear condensates were deposited in Figshare (https://figshare.com/s/ecee627ee1c7d05a91b0). Source data are provided with this paper.

Code availability

The customized Cellprofiler pipeline is described in Supplementary Table 1 and available at https://github.com/madhanicode/sujinlee_cellprofiler. The scripts used to analyze and generate graphs for ChIP-seq data are available at https://github.com/madhanicode/sujinlee_chipseq.

References

45. Chun, C. D. & Madhani, H. D. Applying genetics and molecular biology to the study of the human pathogen *Cryptococcus neoformans*. *Methods Enzymol.* **470**, 797–831 (2010).
46. Burke, J. E. et al. Spliceosome profiling visualizes operations of a dynamic RNP at nucleotide resolution. *Cell* **173**, 1014–1030.e17 (2018).
47. Erdős, G., Pajkos, M. & Dosztányi, Z. IUPred3: prediction of protein disorder enhanced with unambiguous experimental annotation and visualization of evolutionary conservation. *Nucleic Acids Res.* **49**, W297–W303 (2021).
48. Jones, P. et al. InterProScan 5: genome-scale protein function classification. *Bioinformatics* **30**, 1236–1240 (2014).
49. Simm, D., Hatje, K. & Kollmar, M. Waggawagga: comparative visualization of coiled-coil predictions and detection of stable single α-helices (SAH domains). *Bioinformatics* **31**, 767–769 (2015).
50. Trigg, J., Gutwin, K., Keating, A. E. & Berger, B. Multicoil2: predicting coiled coils and their oligomerization states from sequence in the twilight zone. *PLoS ONE* **6**, e23519 (2011).
51. Holehouse, A. S., Das, R. K., Ahad, J. N., Richardson, M. O. G. & Pappu, R. V. CIDER: resources to analyze sequence-ensemble relationships of intrinsically disordered proteins. *Biophys. J.* **112**, 16–21 (2017).
52. Martin, M. Cutadapt removes adapter sequences from high-throughput sequencing reads. *EMBnet.journal* **17**, 10 (2011).
53. Langmead, B., Trapnell, C., Pop, M. & Salzberg, S. L. Ultrafast and memory-efficient alignment of short DNA sequences to the human genome. *Genome Biol.* **10**, R25 (2009).
54. Li, H. et al. The sequence alignment/map format and SAMtools. *Bioinformatics* **25**, 2078–2079 (2009).
55. Quinlan, A. R. & Hall, I. M. BEDTools: a flexible suite of utilities for comparing genomic features. *Bioinformatics* **26**, 841–842 (2010).
56. Koulouras, G. et al. EasyFRAP-web: a web-based tool for the analysis of fluorescence recovery after photobleaching data. *Nucleic Acids Res.* **46**, W467–W472 (2018).

Acknowledgements

We thank members of the Madhani laboratory for helpful discussions and G. J. Narlikar, R. Pappu, D. Canzio and P. A. Dumesic for critical reading of the manuscript. We thank S. Lei for help with making a figure, T. Lou for help with condensate assays, M. Jaime-Garza for help with the mass photometer, K. Herrington and S.Y. Kim at the Center for Advanced Light Microscopy (UCSF) for technical advice. Sequencing was performed at the UCSF CAT, supported by UCSF PBBR, RRP IMIA and National Institutes of Health (NIH; grant no. 1S10OD028511-01). This work was supported by the US NIH (grant no. R01GM71801 to H.D.M.).

Author contributions

S.L. and H.D.M. designed the experiments and wrote the manuscript. H.D.M. supervised all aspects of this work. S.L. performed most of the experiments and analyzed the data. S.A.-A. and K.-J.A. performed and supervised purification of the recombinant PRC2 and histone methyltransferase assay. A.G. generated a customized CellProfiler pipeline to analyze nuclear foci. D.S.P. performed analysis of nuclear foci and ChIP–seq. M.Y.H. analyzed ChIP–seq. B.R. helped with protein purification and ChIP. J.K.D., J.J.M. and J.R.Y. performed, analyzed and supervised MS.

Competing interests

The authors declare no competing interests.

Additional information

Extended data is available for this paper at https://doi.org/10.1038/s41594-023-01000-z.

Supplementary information The online version contains supplementary material available at https://doi.org/10.1038/s41594-023-01000-z.

Correspondence and requests for materials should be addressed to Hiten D. Madhani.

Peer review information *Nature Structural & Molecular Biology* thanks the anonymous reviewers for their contribution to the peer review of this work. Sara Osman and Dimitris Typas were the primary editors on this article and managed its editorial process and peer review in collaboration with the rest of the editorial team.

https://doi.org/10.1038/s41594-023-01000-z

a

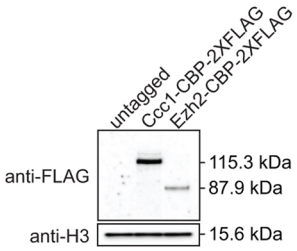

b

Ccc1-CBP-2XFLAG	
CNAG	Name
00083	**Ccc1**
01563	Clr3
04790	Eza1

c

Ezh2-CBP-2XFLAG	
CNAG	Name
07553	**Ezh2**
02345	**Eed1**
07433	**Bnd1**
03297	**Msl1**
04762	Ras2
01920	polyubiquitin
06125	TEF1 alpha
05556	
03959	
01170	

Extended Data Fig. 1 | Ccc1 is not a tightly bound core subunit of PRC2 complex. (a) Expression of endogenous Ccc1 and Ezh2 with a C-terminal CBP-2XFLAG tag, as assessed by western blotting using the antibodies indicated on the left. H3 serves as a loading control. Data are representative of two independent experiments. Protein interaction partners of **(b)** Ccc1 and **(c)** Ezh2. Each bait protein was purified by tandem affinity purification following DNase treatment and its protein interaction partners were determined by mass spectrometry. Subunits of the PRC2 complex are indicated in bold. Likely contaminants have been excluded (Supplementary Table 4).

https://doi.org/10.1038/s41594-023-01000-z

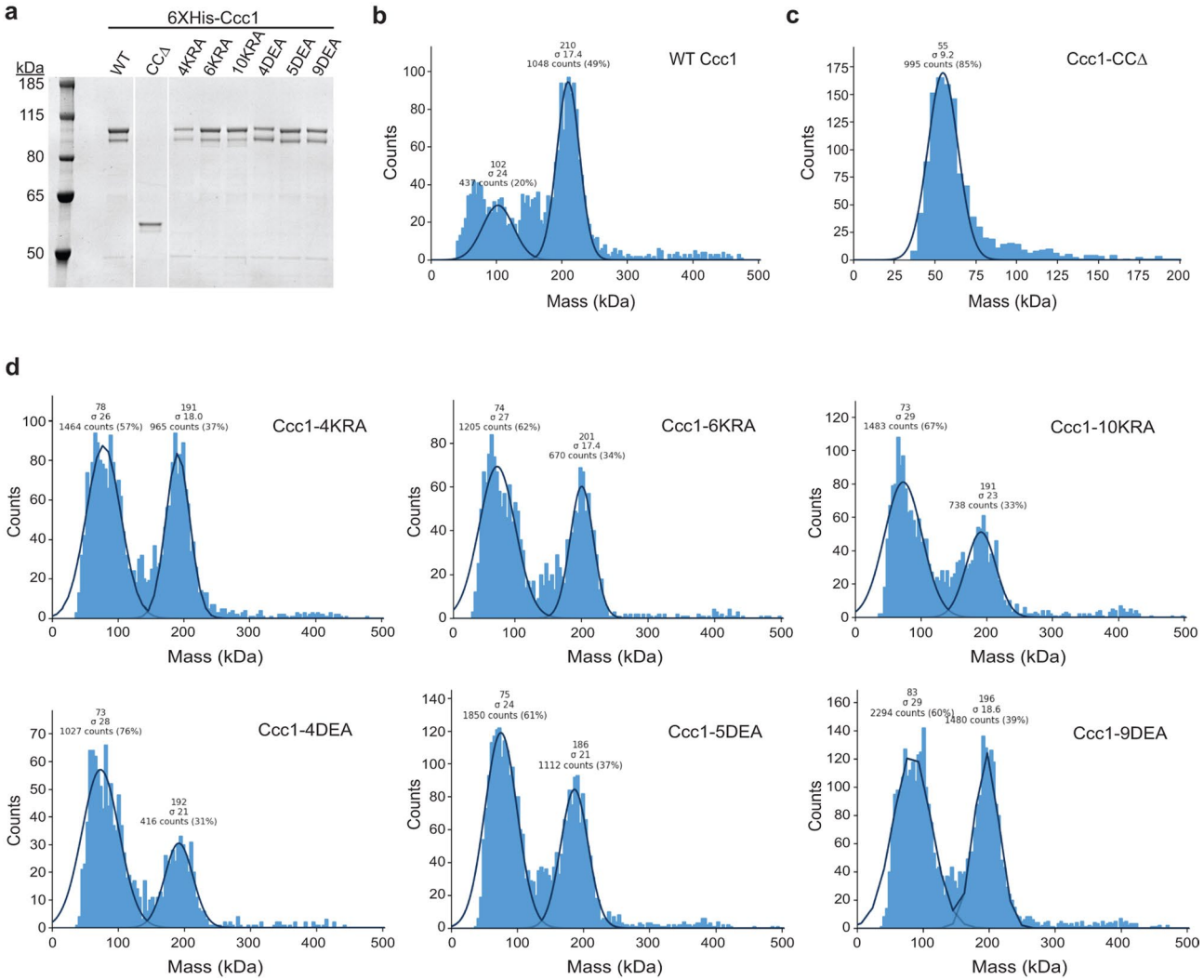

Extended Data Fig. 2 | Determination of oligomerization status of purified Ccc1 wild-type and mutants. (a) Purified 6XHis-Ccc1 wild-type, C-terminally truncated Ccc1-CCΔ (1-434 amino acids), and IDR mutants. Data are representative of three independent experiments. Mass photometry analysis of **(b)** Ccc1 wild-type, **(c)** Ccc1-CCΔ, **(d)** Ccc1 IDR mutants in 20 mM HEPES, pH 7.5, and 250 mM NaCl.

https://doi.org/10.1038/s41594-023-01000-z

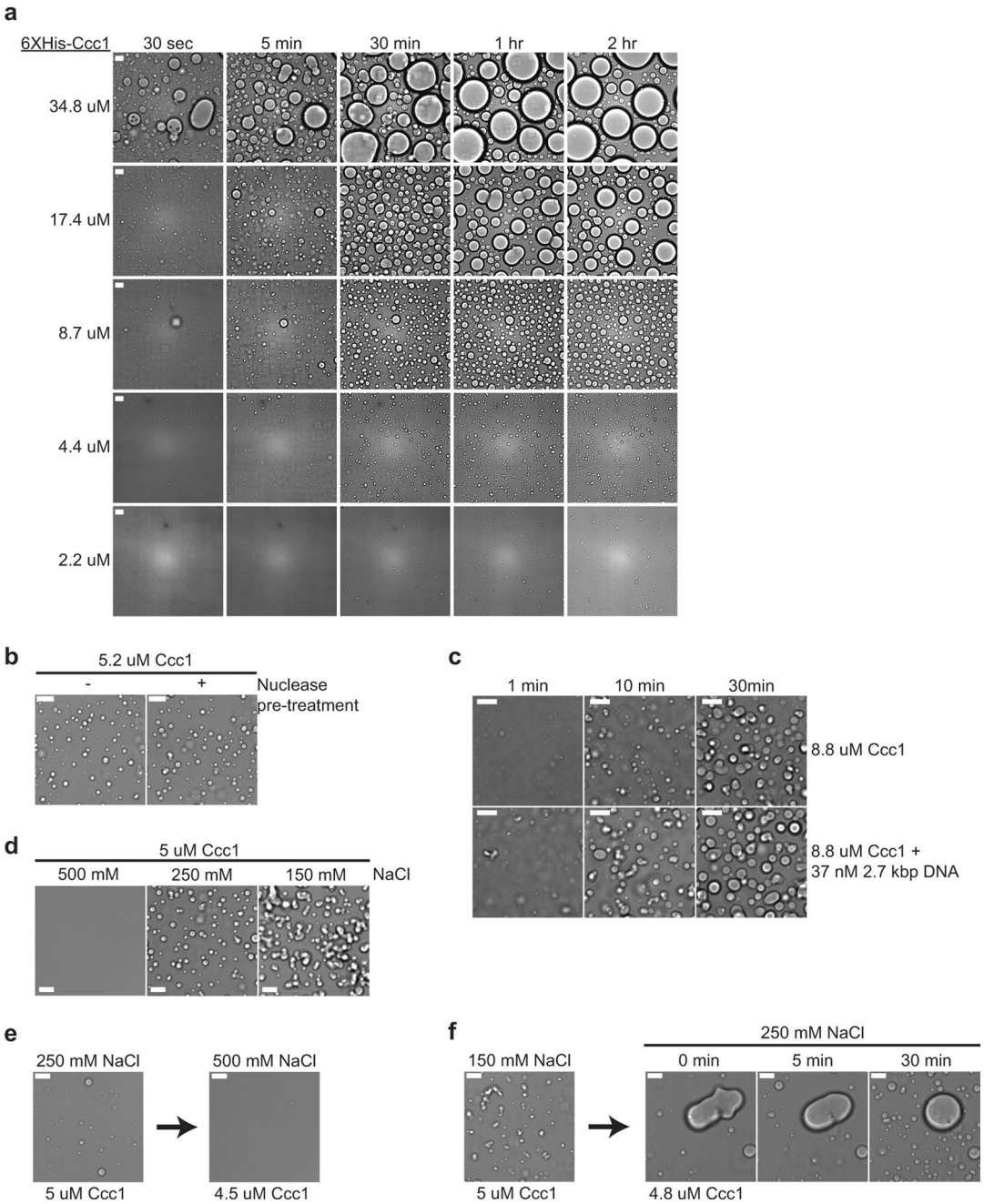

Extended Data Fig. 3 | Ccc1 undergoes phase separation *in vitro* and forms liquid-like droplets. (a) DIC images of concentration-dependent wild-type Ccc1 condensate formation in 20 mM HEPES, pH 7.5, and 250 mM NaCl. Scale bars, 10 µm. **(b)** Ccc1 condensate formation with or without prior nuclease treatment. For nuclease treatment, 20 µl of 20 µM Ccc1 was incubated with 1 µl of TURBO DNase (2 U/µl) and 1 µl of RNase A (10 mg/ml) at RT for 1 h. Scale bars, 10 µm. **(c)** Ccc1 condensate formation in the presence of 2.7 kbp DNA. Scale bars, 10 µm. **(d)** Salt-dependent Ccc1 condensate formation. Phase separation of 5 µM Ccc1 was induced for 30 min in 20 mM HEPES, pH 7.5, buffer containing 500, 250, and 150 mM NaCl. Scale bars, 10 µm. **(e)** Salt-dependent reversibility of Ccc1 condensate formation. After 10 min induction of condensate formation in 20 mM HEPES, pH 7.5, and 250 mM NaCl, NaCl concentration of buffer was adjusted to 500 mM. Scale bars, 10 µm. **(f)** After 10 min induction of condensate formation in 20 mM HEPES, pH 7.5, and 150 mM NaCl, NaCl concentration of buffer was adjusted to 250 mM. Scale bars, 10 µm. Data are representative of three (**a**, **d**, **e**, **f**) or two (**b**, **c**) independent experiments.

https://doi.org/10.1038/s41594-023-01000-z

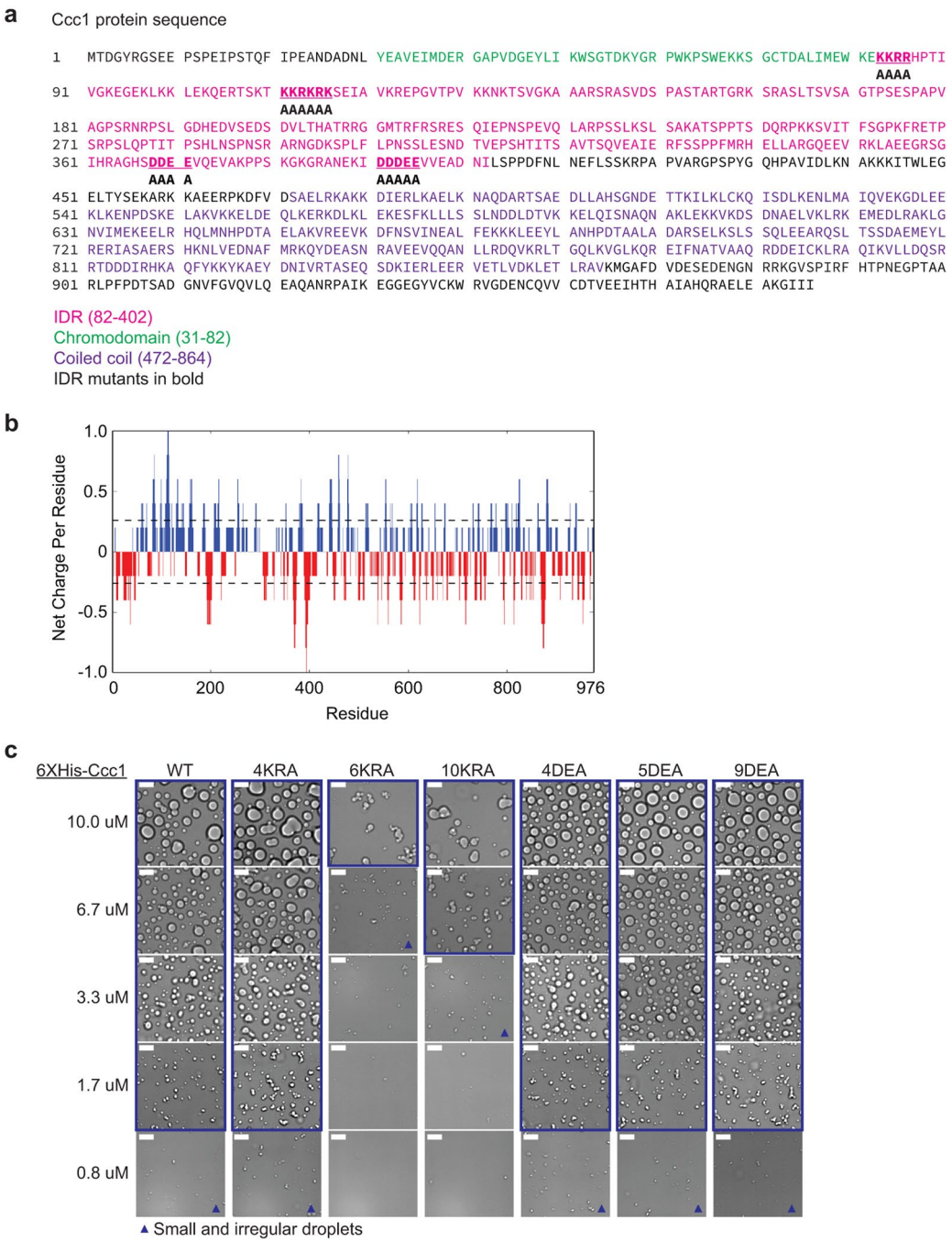

Extended Data Fig. 4 | Ccc1 phase separation is programmed by two basic charged clusters in IDR. (a) Ccc1 protein sequence. IDR, chromodomain, coiled-coil, and IDR mutation sites are as indicated. **(b)** Ccc1 charge distribution. **(c)** Concentration-dependent condensate formation of Ccc1 wild-type and IDR mutants in 20 mM HEPES, pH 7.5, and 250 mM NaCl after 2 h of plating. Scale bars, 10 μm. Data are representative of three independent experiments.

https://doi.org/10.1038/s41594-023-01000-z

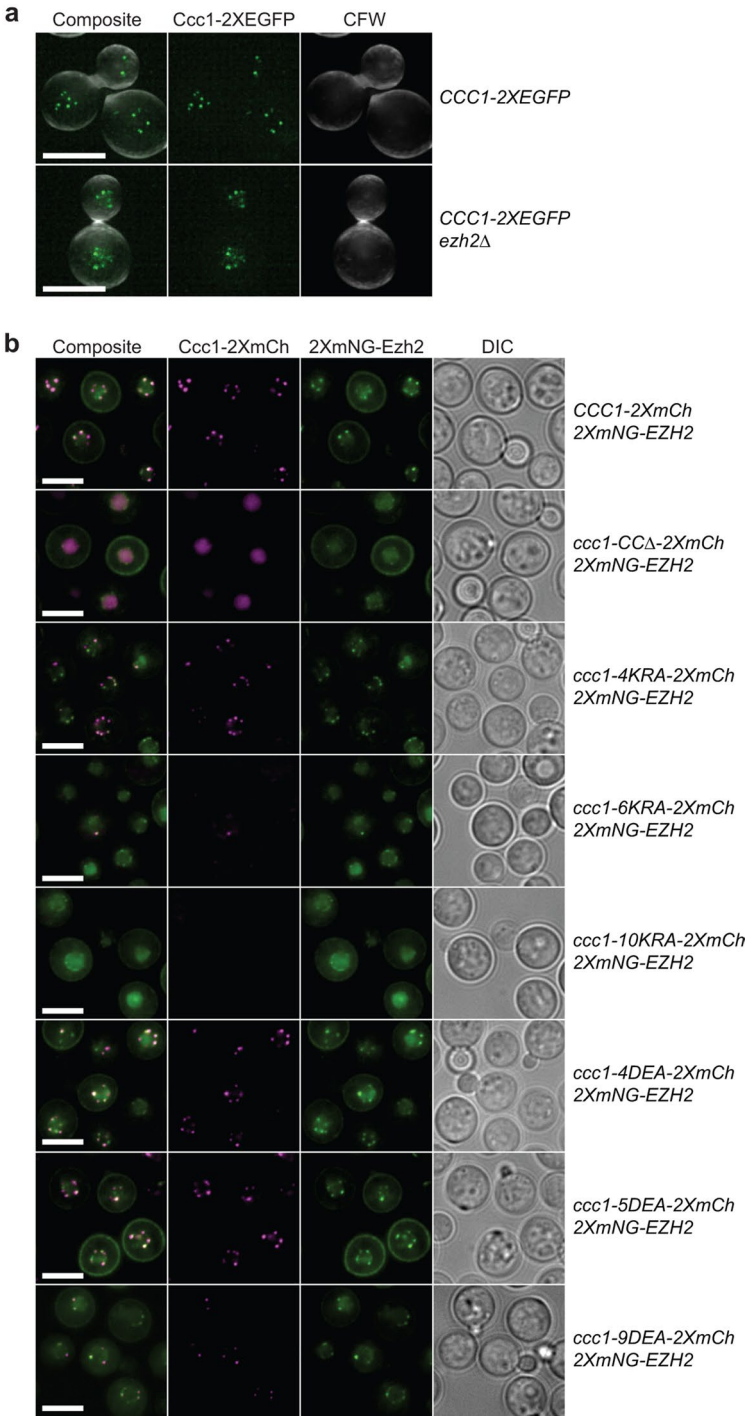

Extended Data Fig. 5 | Ccc1 foci are enriched for Ezh2. (a) Live cell images of Ccc1-2XEGFP foci in the wild-type and *ezh2Δ*. Scale bars, 5 µm. **(b)** Live cell images of cells expressing 2XmNeonGreen-Ezh2 and Ccc1 variants tagged with 2XmCherry. Scale bars, 5 µm. Data in **a** and **b** are representative of three independent experiments.

https://doi.org/10.1038/s41594-023-01000-z

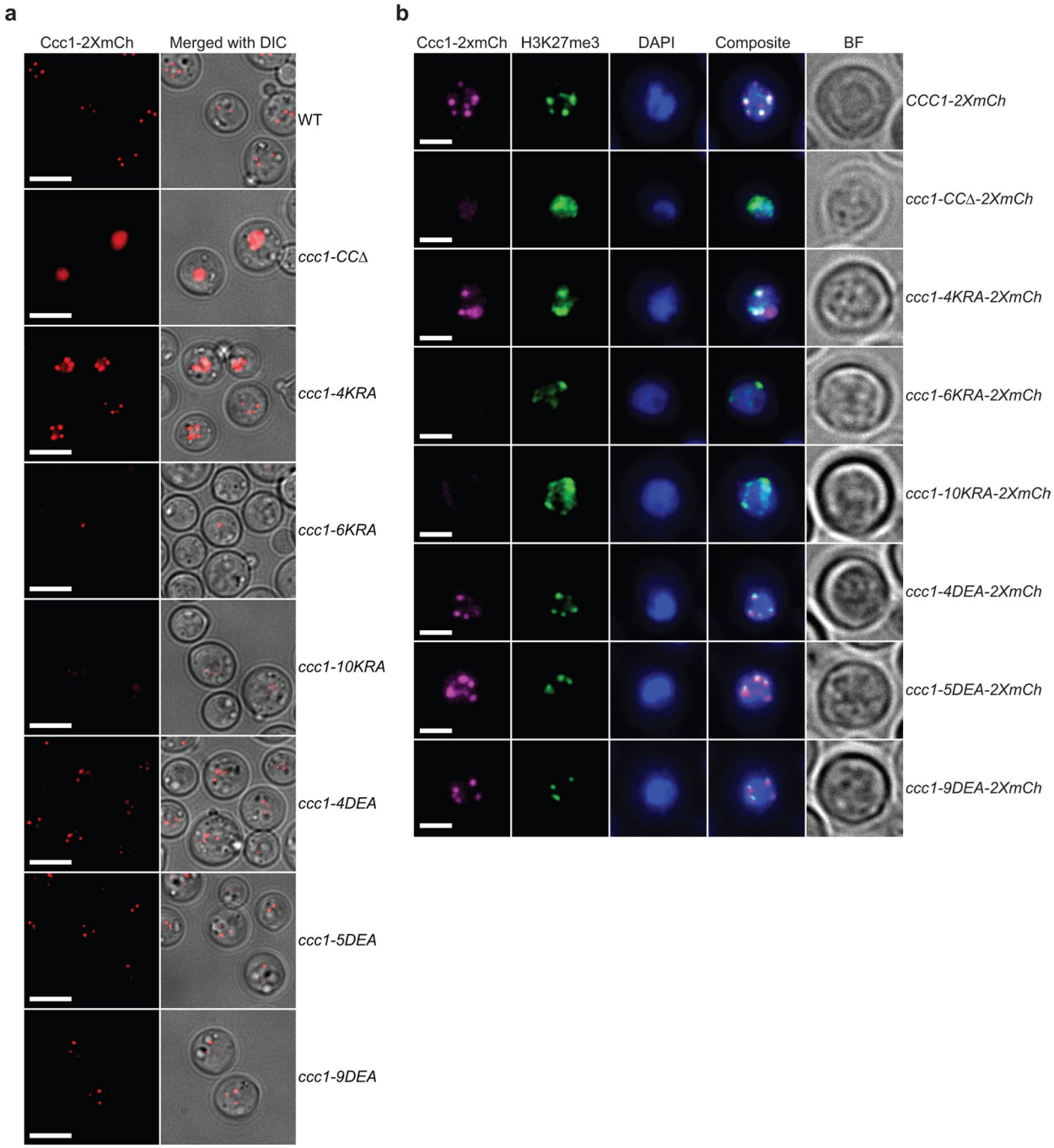

Extended Data Fig. 6 | Ccc1 foci are colocalized with H3K27me3. (a) Live cell images of Ccc1 variants tagged with 2XmCherry. Scale bars, 5 µm. **(b)** Distribution of H3K27me3 in cells expressing Ccc1 variants tagged with 2XmCherry. Scale bars, 2 µm. Data in **a** and **b** are representative of three independent experiments.

https://doi.org/10.1038/s41594-023-01000-z

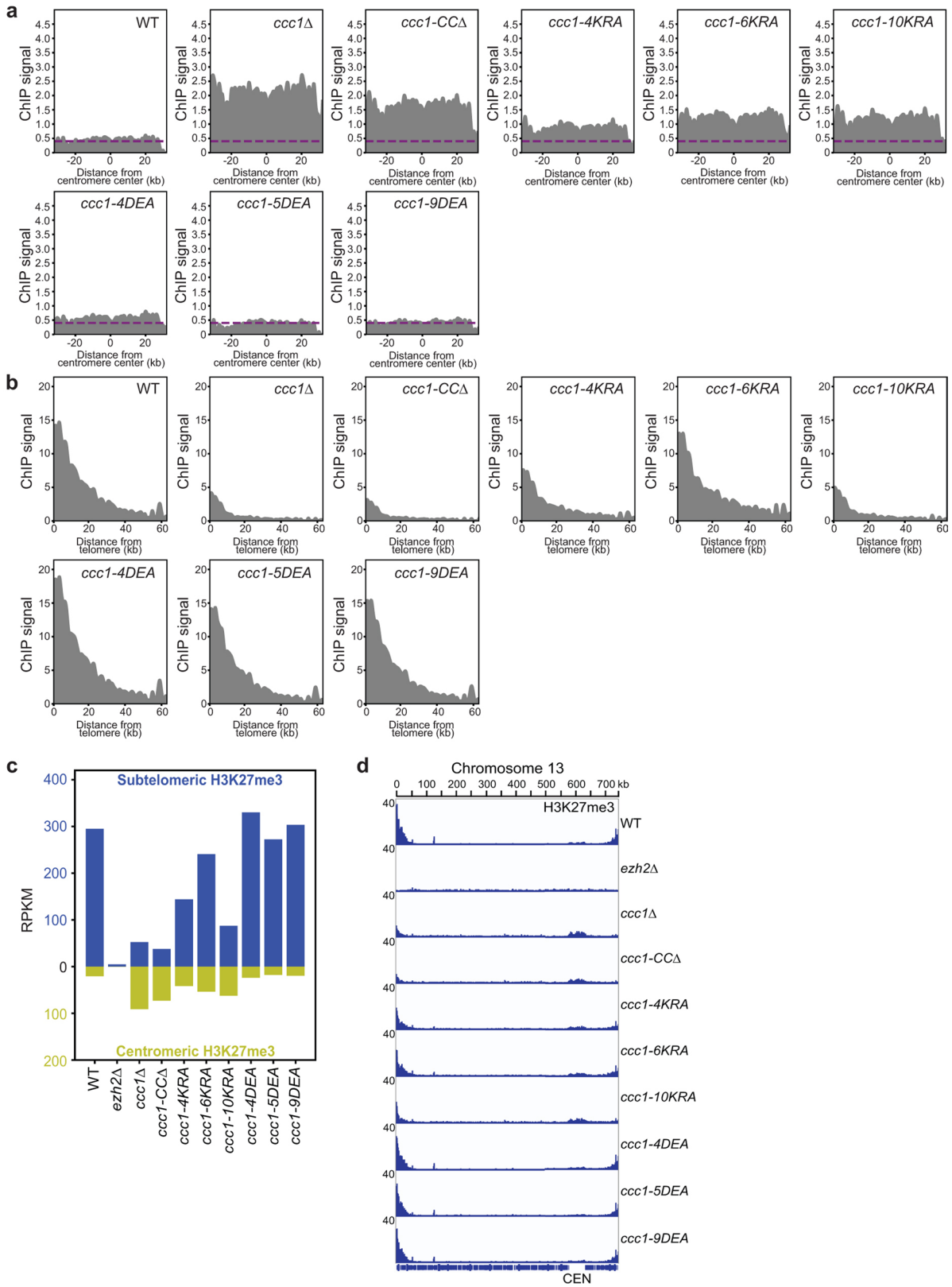

Extended Data Fig. 7 | ChIP-seq analysis of the replicate sequencing libraries. **(a)** Average centromeric H3K27me3. **(b)** Average subtelomeric H3K27me3. **(c)** H3K27me3 at subtelomeric (blue bar) versus centromeric regions (green bar) as measured by ChIP-seq. Density (RPKM) of signal above background is reported. **(d)** ChIP-seq traces of H3K27me3 signal across chromosome 13 in cells expressing Ccc1 variants or cells lacking Ccc1 or Ezh2.

https://doi.org/10.1038/s41594-023-01000-z

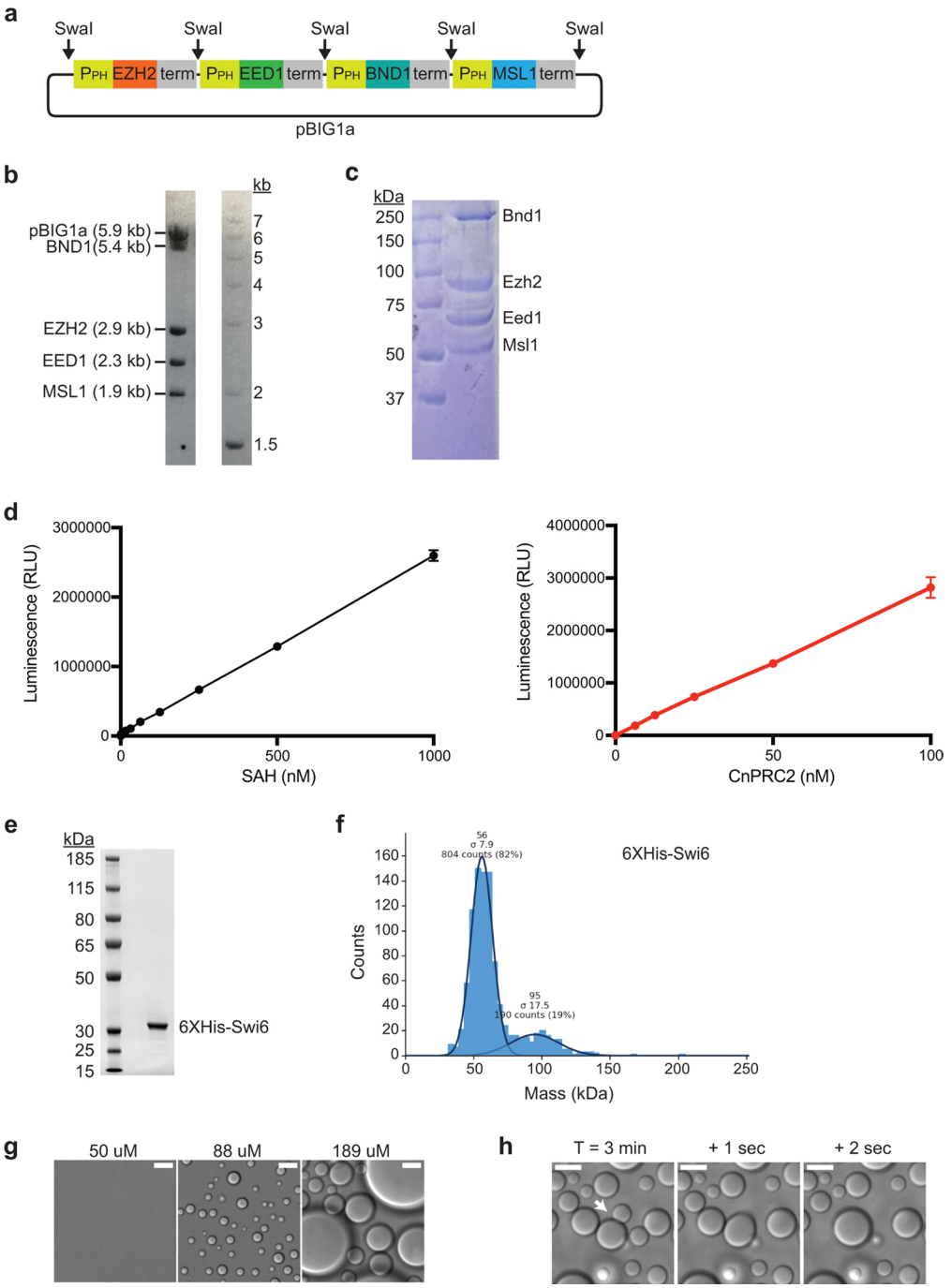

Extended Data Fig. 8 | Purification of catalytically active PRC2 complex and Swi6. (a) Schematic representation of the PRC2 coexpression construct. Each gene expression cassette contains a polyhedrin promoter (P_{PH}), a cDNA of the PRC2 component, and an SV40 terminator (term). The cDNAs are tagged as follows: 3XStrep-TagII-HRV3C-EZH2, 9XHis-HRV3C-EED1, FLAG-HRV3C-BND1, and 6XHis-TEV-MSL1. **(b)** Agarose gel of SwaI-digested construct in (a). **(c)** Coomassie stained SDS-polyacrylamide gel of the purified recombinant PRC2. **(d)** (Left) SAH standard curve (Right) Histone Methyltransferase assay of the recombinant PRC2 on the nucleosome assembled with *Xenopus* histone H3 (28SAPAT32 replaced for 28QTTTSAAA34 of *C. neoformans* histone H3). (Mean ± SEM, n = 3 independent replicates) **(e)** Purified 6XHis-Swi6. **(f)** Mass photometry analysis of Swi6 in 20 mM HEPES, pH 7.5, and 150 mM NaCl. **(g)** DIC images of concentration-dependent Swi6 condensate formation in 20 mM HEPES, pH 7.5, and 125 mM NaCl 30 min after plating. Scale bars, 10 µm. **(h)** Condensate fusion of 189 µM Swi6 at indicated time points. Scale bars, 10 µm. Data in **b**, **c**, **e**, **g**, and **h** are representative of three independent experiments.

nature portfolio

Corresponding author(s): Hiten D. Madhani

Last updated by author(s): Mar 27, 2023

Reporting Summary

Nature Portfolio wishes to improve the reproducibility of the work that we publish. This form provides structure for consistency and transparency in reporting. For further information on Nature Portfolio policies, see our Editorial Policies and the Editorial Policy Checklist.

Statistics

For all statistical analyses, confirm that the following items are present in the figure legend, table legend, main text, or Methods section.

n/a	Confirmed
☐	☒ The exact sample size (*n*) for each experimental group/condition, given as a discrete number and unit of measurement
☒	☐ A statement on whether measurements were taken from distinct samples or whether the same sample was measured repeatedly
☐	☒ The statistical test(s) used AND whether they are one- or two-sided *Only common tests should be described solely by name; describe more complex techniques in the Methods section.*
☒	☐ A description of all covariates tested
☒	☐ A description of any assumptions or corrections, such as tests of normality and adjustment for multiple comparisons
☐	☒ A full description of the statistical parameters including central tendency (e.g. means) or other basic estimates (e.g. regression coefficient) AND variation (e.g. standard deviation) or associated estimates of uncertainty (e.g. confidence intervals)
☐	☒ For null hypothesis testing, the test statistic (e.g. *F*, *t*, *r*) with confidence intervals, effect sizes, degrees of freedom and *P* value noted *Give P values as exact values whenever suitable.*
☒	☐ For Bayesian analysis, information on the choice of priors and Markov chain Monte Carlo settings
☒	☐ For hierarchical and complex designs, identification of the appropriate level for tests and full reporting of outcomes
☐	☒ Estimates of effect sizes (e.g. Cohen's *d*, Pearson's *r*), indicating how they were calculated

Our web collection on statistics for biologists contains articles on many of the points above.

Software and code

Policy information about availability of computer code

Data collection	Microscopy data were acquired with NIS-Elements and Micro-Manager. Prediction of protein disorder and structured domains was performed using IUPred3, InterProScan5, Waggawagga and Multicoil2. Charge distribution of protein was calculated using CIDER.
Data analysis	Microscopy data were analyzed in Fiji and CellProfiler using a custom-made pipeline described in the Supplementary Table 1 and available at https://github.com/madhanicode/sujinlee_cellprofiler. Data analyses were conducted using GraphPad Prism 9.

For manuscripts utilizing custom algorithms or software that are central to the research but not yet described in published literature, software must be made available to editors and reviewers. We strongly encourage code deposition in a community repository (e.g. GitHub). See the Nature Portfolio guidelines for submitting code & software for further information.

Data

Policy information about availability of data

All manuscripts must include a data availability statement. This statement should provide the following information, where applicable:

- Accession codes, unique identifiers, or web links for publicly available datasets
- A description of any restrictions on data availability
- For clinical datasets or third party data, please ensure that the statement adheres to our policy

ChIP-seq data were deposited in the Gene Expression Omnibus under accession number GSE195824. Live cell imaging data to quantify nuclear condensates were uploaded to figshare. Source data are provided with the manuscript.

Field-specific reporting

Please select the one below that is the best fit for your research. If you are not sure, read the appropriate sections before making your selection.

☒ Life sciences ☐ Behavioural & social sciences ☐ Ecological, evolutionary & environmental sciences

For a reference copy of the document with all sections, see nature.com/documents/nr-reporting-summary-flat.pdf

Life sciences study design

All studies must disclose on these points even when the disclosure is negative.

Sample size	The sample sizes are indicated in the figure legends. Sample sizes were determined based on our experience (Dumesic et al., DOI 10.1016/j.cell.2014.11.039) and accepted practice in the field balancing statistical robustness and available resources.
Data exclusions	Protein hits filtered out from the mass spectrometry results are given in Supplementary Table 4. For the analysis of nuclear condensates, foci contained within a cell were retained and all others were filtered out.
Replication	All conclusions were based on findings reproduced in triplicated or at least duplicated experiments.
Randomization	Not relevant. All experiments involved comparison of isogenic wild type and mutants.
Blinding	Microscopy data collection was guided by blinded investigators.

Reporting for specific materials, systems and methods

We require information from authors about some types of materials, experimental systems and methods used in many studies. Here, indicate whether each material, system or method listed is relevant to your study. If you are not sure if a list item applies to your research, read the appropriate section before selecting a response.

Materials & experimental systems

n/a	Involved in the study
☐	☒ Antibodies
☐	☒ Eukaryotic cell lines
☒	☐ Palaeontology and archaeology
☒	☐ Animals and other organisms
☒	☐ Human research participants
☒	☐ Clinical data
☒	☐ Dual use research of concern

Methods

n/a	Involved in the study
☐	☒ ChIP-seq
☒	☐ Flow cytometry
☒	☐ MRI-based neuroimaging

Antibodies

Antibodies used	Rabbit Polyclonal Anti-GFP (1:3000, Abcam ab290) GFP Tag Polyclonal Antibody (1:3000, Invitrogen A11122) Histone H3 Polyclonal Antibody (1:1000, Invitrogen PA5-16183) Goat Anti-Rabbit IgG (H + L)-HRP Conjugate (1:20000, Bio-Rad 1706515) Anti-H3K27me3 (1:100 for immunofluorescence, This laboratory) Goat Anti-Rabbit IgG H&L (Alexa Fluor 488) preadsorbed (1:1000, Abcam ab150085)
Validation	All antibodies used in this study except anti-H3K27me3 are commercially available and have been validated by the manufacturer. See information associated with catalog numbers: https://www.abcam.com/products/primary-antibodies/gfp-antibody-ab290.html?productWallTab=ShowAll, https://www.thermofisher.com/antibody/product/GFP-Antibody-Polyclonal/A-11122, https://www.thermofisher.com/antibody/product/Histone-H3-Antibody-Polyclonal/PA5-16183, https://www.bio-rad.com/en-us/sku/1706515-goat-anti-rabbit-igg-h-l-hrp-conjugate?ID=1706515, https://www.abcam.com/products/secondary-antibodies/goat-rabbit-igg-hl-alexa-fluor-488-preadsorbed-ab150085.html Anti-H3K27me3 was previously validated in studies of our laboratory (Dumesic et al., DOI 10.1016/j.cell.2014.11.039).

Eukaryotic cell lines

Policy information about cell lines

Cell line source(s)	Sources of yeast strains are given in the Supplementary Table 2. Sf9 cells for expression of recombinant PRC2 were from Thermo Fisher.

Authentication	Yeast strains were verified by PCR and Sanger sequencing. Sf9 cells were prepared as serum-free, suspension cultures from Sf9 cells that originated at the USDA Insect Pathology Laboratory. Sf9 cells certificates of analysis are available at https://www.thermofisher.com/order/catalog/product/11496015.
Mycoplasma contamination	Not applicable for yeast strains. Sf9 cells tested negative for mycoplasma contamination.
Commonly misidentified lines (See ICLAC register)	No commonly misidentified cell lines were used in the study.

ChIP-seq

Data deposition

☒ Confirm that both raw and final processed data have been deposited in a public database such as GEO.

☒ Confirm that you have deposited or provided access to graph files (e.g. BED files) for the called peaks.

Data access links *May remain private before publication.*	https://www.ncbi.nlm.nih.gov/geo/query/acc.cgi?acc=GSE195824
Files in database submission	Raw files: WCE-SL372_S29_L004_R1_001.fastq.gz WCE-CK2308_S28_L004_R1_001.fastq.gz WCE-CK6644_S27_L004_R1_001.fastq.gz WCE-SL362_S33_L004_R1_001.fastq.gz WCE-SL363_S34_L004_R1_001.fastq.gz WCE-SL364_S35_L004_R1_001.fastq.gz WCE-SL365_S36_L004_R1_001.fastq.gz WCE-SL366_S37_L004_R1_001.fastq.gz WCE-SL367_S38_L004_R1_001.fastq.gz WCE-SL369_S32_L004_R1_001.fastq.gz H3K27me3-R1-SL372_S43_L004_R1_001.fastq.gz H3K27me3-R1-CK2308_S42_L004_R1_001.fastq.gz H3K27me3-R1-CK6644_S41_L004_R1_001.fastq.gz H3K27me3-R1-SL362_S52_L005_R1_001.fastq.gz H3K27me3-R1-SL363_S46_L004_R1_001.fastq.gz H3K27me3-R1-SL364_S47_L004_R1_001.fastq.gz H3K27me3-R1-SL365_S48_L004_R1_001.fastq.gz H3K27me3-R1-SL366_S49_L004_R1_001.fastq.gz H3K27me3-R1-SL367_S53_L005_R1_001.fastq.gz H3K27me3-R1-SL369_S45_L004_R1_001.fastq.gz H3K27me3-R2-SL372_S57_L005_R1_001.fastq.gz H3K27me3-R2-CK2308_S56_L005_R1_001.fastq.gz H3K27me3-R2-CK6644_S55_L005_R1_001.fastq.gz H3K27me3-R2-SL362_S61_L005_R1_001.fastq.gz H3K27me3-R2-SL363_S62_L005_R1_001.fastq.gz H3K27me3-R2-SL364_S63_L005_R1_001.fastq.gz H3K27me3-R2-SL365_S64_L005_R1_001.fastq.gz H3K27me3-R2-SL366_S65_L005_R1_001.fastq.gz H3K27me3-R2-SL367_S66_L005_R1_001.fastq.gz H3K27me3-R2-SL369_S60_L005_R1_001.fastq.gz Processed files: H3K27me3-R1-SL372_S43_L004_R1_001_multi_sorted_norm_500bp_smooth.bedgraph H3K27me3-R1-CK2308_S42_L004_R1_001_multi_sorted_norm_500bp_smooth.bedgraph H3K27me3-R1-CK6644_S41_L004_R1_001_multi_sorted_norm_500bp_smooth.bedgraph H3K27me3-R1-SL362_S52_L005_R1_001_multi_sorted_norm_500bp_smooth.bedgraph H3K27me3-R1-SL363_S46_L004_R1_001_multi_sorted_norm_500bp_smooth.bedgraph H3K27me3-R1-SL364_S47_L004_R1_001_multi_sorted_norm_500bp_smooth.bedgraph H3K27me3-R1-SL365_S48_L004_R1_001_multi_sorted_norm_500bp_smooth.bedgraph H3K27me3-R1-SL366_S49_L004_R1_001_multi_sorted_norm_500bp_smooth.bedgraph H3K27me3-R1-SL367_S53_L005_R1_001_multi_sorted_norm_500bp_smooth.bedgraph H3K27me3-R1-SL369_S45_L004_R1_001_multi_sorted_norm_500bp_smooth.bedgraph H3K27me3-R2-SL372_S57_L005_R1_001_multi_sorted_norm_500bp_smooth.bedgraph H3K27me3-R2-CK2308_S56_L005_R1_001_multi_sorted_norm_500bp_smooth.bedgraph H3K27me3-R2-CK6644_S55_L005_R1_001_multi_sorted_norm_500bp_smooth.bedgraph H3K27me3-R2-SL362_S61_L005_R1_001_multi_sorted_norm_500bp_smooth.bedgraph H3K27me3-R2-SL363_S62_L005_R1_001_multi_sorted_norm_500bp_smooth.bedgraph H3K27me3-R2-SL364_S63_L005_R1_001_multi_sorted_norm_500bp_smooth.bedgraph H3K27me3-R2-SL365_S64_L005_R1_001_multi_sorted_norm_500bp_smooth.bedgraph H3K27me3-R2-SL366_S65_L005_R1_001_multi_sorted_norm_500bp_smooth.bedgraph H3K27me3-R2-SL367_S66_L005_R1_001_multi_sorted_norm_500bp_smooth.bedgraph H3K27me3-R2-SL369_S60_L005_R1_001_multi_sorted_norm_500bp_smooth.bedgraph

Genome browser session (e.g. UCSC)	No longer applicable.

Methodology

Replicates	Two individual replicates per genotype were analyzed.
Sequencing depth	11~18 millions of single-end reads (50bp) per replicate per genotype. Multiple alignments were allowed to analyze repetitive reads.
Antibodies	Anti-H3K27me3 (Dumesic et al., DOI 10.1016/j.cell.2014.11.039)
Peak calling parameters	Bowtie was used for alignment with modified parameters (-v2, -M1, --best) to allow multiple alignments and random assignment. No peak calling was performed.
Data quality	Data quality was assessed by FastQC.
Software	Sequencing reads were trimmed for adaptor sequence using Cutadapt and aligned to the C. neoformans genome using Bowtie (modified parameters: -v2, -M1, --best). Alignment files were sorted and indexed using SAMtools and bedgraph files were generated using BEDTools. Each bedgraph file was scaled by million aligned reads, normalized to the corresponding whole cell extract at each genomic position, and smoothed using a 500 bp centered rolling mean using custom Python scripts. https://github.com/madhanicode/sujinlee_chipseq